RESEARCH ARTICLE





Simultaneous topology and machine orientation optimization for multiaxis machining

Joshua Gasick | Xiaoping Qian®

Department of Mechanical Engineering, University of Wisconsin-Madison, Madison, Wisconsin, USA

Correspondence

Xiaoping Qian, Department of Mechanical Engineering, University of Wisconsin-Madison, Madison, WI 53706-1572, USA. Email: qian@engr.wisc.edu

Funding information

Office of Naval Research, Grant/Award Number: N00014-18-1-2685

Abstract

We present a density-based topology optimization approach for multi-axis machining where optimized designs can be machined by one or multiple axes. In our approach, density and machine axes can be simultaneously optimized. The fulcrum of our multi-axis machinability based topology optimization approach is a formulation that characterizes machinability through inaccessible volume. This formulation is differentiable to both density and machining axes, and thus is amenable to gradient-based optimization. We use an advection-diffusion equation to facilitate the evaluation of inaccessible volume. Numerical examples on 2D and 3D linear elasticity problems are presented as a demonstration of the efficacy of this approach.

KEYWORDS

advection-diffusion equation, manufacturability for machining, topology optimization

1 | INTRODUCTION

Topology optimization is a computational approach to generating optimal structures subjected to physical loading. Expanding from its origins as a structural design method,¹ topology optimization (TO) has since been applied to various problems including those of heat conduction,² electromagnetics,³ and thermal-fluids.^{4,5} Some popular TO methods include the density-based method,⁶ evolutionary structural optimization,⁷ and the level-set method.⁸

While TO designs generally offer high computationally-predicted performance, they can also be arbitrarily shaped which complicates their physical realization. Recent developments in the field of additive manufacturing have introduced the possibility of capturing these benefits by precisely re-creating the sometimes byzantine geometries that TO can yield. However, additive manufacturing (AM) remains a developing discipline, and particularly on the bases of cost, time to manufacture, surface quality, and volume production, AM remains an intriguing but often less desirable alternative to traditional manufacturing methods such as machining, molding, and casting. In particular, multi-axis machining utilizes a sufficiently augmented number of degrees of freedom compared to 2.5D machining, 3-axis machining, and other conventional manufacturing methods to establish it as a viable vehicle for achieving an appropriate compromise between performance and economy. Coupling the flexibility of multi-axis machining with the ability of topology optimization to more fully explore the bounds of a design space obviates the need for trial-and-error based design techniques when developing manufacturable geometries.

The generation of geometries that are simultaneously optimally suited for a system of physical loadings and that can be feasibly produced through traditional manufacturing methods is an ongoing area of research. For example, Reference 11 considers the requirements for turning, milling, and casting operations in addition to techniques for attaining manufacturable designs. Zhu and Guest applied a projection based scheme to restrict the design space such that the density monotonically increased in the direction of milling, ensuring manufacturability. Gersborg and Andreasen used a

re-parametrization of the design density in the context of casting constraints to achieve a similar end.¹³ For 2.5D machining, Liu and Ma used a feature fitting algorithm to ensure that in a final design, the material to be removed could be described as a set of parametrized primitive shapes and thus could be successfully created.¹⁴ A Heaviside projection-based method was used in Reference 15 to prevent small, non-manufacturable solid and void features from forming. Using the level set method, manufacturability for extrusion was considered in Reference 16. Additionally, minimal length scale control¹⁷⁻¹⁹ and maximal feature size^{20,21} have been investigated.

Particular to machining considerations, a work by Langelaar introduced a machining filter based on a cumulative summation of the density in the direction of machining which addressed tool length, tool shape, and feature accessibility concerns.²² A subsequent method created Mirzendehdel et al. involved an inaccessibility measure field defined through the evaluation of a convolution field which was similarly extensible to multiples axes.²³ However, neither of these publications have included the machining direction(s) as a degree of freedom during optimization, and thus the identified optimal calculated cost pertains specifically to the chosen orientation.

A method for optimizing the manufacturing orientation (the build direction) in an additive manufacturing environment was formulated in Reference 24 in an effort to limit the support structure required to form the part. This approach led to the creation of higher performance designs with respect to optimizations for which the build direction was pre-selected. Since the manufacturing orientation is a salient factor in design performance in both additive and subtractive manufacturing contexts, it is desirable to allow the axes of machining to organically evolve over the course of the optimization to avoid imposing an arbitrarily intrusive constraint on the developing structure. The utility of our inaccessible volume approach originates from its differentiability with respect to both the density and the orientation(s) of machining. This makes the approach amenable for use in a gradient-based TO, wherein both the density and the machine axes are cast as design variables. In turn, this more fully liberates design evolution from designer intuition and aids in the avoidance of inferior designs which can result from the aforementioned imposition of machining constraints that use pre-selected machining orientations. To achieve this differentiability, our method employs the use of a pseudo-physical equation via an advection-diffusion equation.

Pseudo-physics or alternative physical models in topology optimization as a method for evaluating manufacturability have been used for a variety of purposes. In Reference 25, a heat problem was solved over the design domain using void regions as source terms and fixing the temperature at the boundaries to identify internal voids. With the density specified to be non-conductive, heat flowed freely out of void regions connected to the boundaries, but aggregated in isolated voids, leading to the straightforward differentiation between internal and external voids volumes. In Reference 26, an advection-diffusion equation was solved to identify geometric features that would inhibit the successful casting of the part and was able to incorporate multiple parting directions. It is this work from which the advection-diffusion equation used for our proposed method of enforcing the multi-axis machinability of a design originates from.

The pseudo-physics approach described subsequently necessitates the solving of one state and one adjoint equation for each machining axis. However, it introduces the possibility of including both the density and the machine axes as design variables in a gradient-based optimization, and as a result we believe that there is sufficient justification for the additional computational resources required.

In this article, we develop a density-based method for identifying inaccessible volumes in a geometric design and thus constraining the optimization to yield only machinable results. To prevent trivial solutions from forming that satisfy the other constraints but are composed extensively of intermediate density, a density grayness constraint is included in the formulation and is discussed thoroughly in Reference 27. For optimizations involving particularly intrusive manufacturing orientations, the typical volume and previously mentioned grayness constraints have been re-cast as exponential constraints to force convergence.

The article is organized as follows: Section 2 introduces the concept of the inaccessible volume, then develops a mathematical expression for use in optimization. Section 3 incorporates this new constraint into a topology optimization formulation to effectively ensure designs are amenable to subtractive manufacturing. Section 4 summarizes the sensitivity of the new constraint. Numerical results and a discussion of the results, advection-diffusion boundary conditions, and the exponential power terms follow in Section 5. Conclusions are drawn in Section 6.

2 | MACHINABILITY ANALYSIS THROUGH INACCESSIBLE VOLUME

This section first describes the concept of an inaccessible volume through the application of an advection-diffusion equation and discusses its physical interpretations. The PDE filtering and Heaviside projection schemes implemented in

this article are then briefly introduced as necessary context prior to the formulation of inaccessible volume. This is followed by the development of a differentiable mathematical expression for inaccessible volume that can be incorporated into topology optimization. This expression can be used to control and constrain non-manufacturability in a geometric design with respect to multi-axis machining.

2.1 | Inaccessible volume

To ensure the machinability of a geometric design, it is sufficient to enforce the condition that all volumes in the original, stock workpiece designated for removal are accessible to at least one machine tool. In this article, machine tools used for removing material from the workpiece originate from outside the domain, and remove material in a strictly axial manner. Thus, the aforementioned condition is violated when a region of stock that is designated to remain as part of the final product obstructs the tool path to a region of the domain that is designated for removal. Machining away this material region from the workpiece to obtain the geometry specified by the design would require the tool piece to somehow pass through a solid without removing material.

In this article, we propose to identify the volume of a domain that a tool piece can directly access through a physical model. For this work, the selected physical model is an advection-diffusion equation subsequently introduced in Section 2.2. For illustration purposes, this equation will be interpreted as a model for light projection.

Figure 1 illustrates key terms and how the application of this physical model aids in identifying machinable and non-machinable volumes in a geometric design for a given tool.

Beginning with Figure 1A, a workpiece is identified which represents both the design domain and the raw stock from which material is removed to create a design. The workpiece in Figure 1A is divided into two volumes in Figure 1B. The first of these is the solid portion of the design, which is the material specified to remain after machining. The second is the void, which corresponds to the portion of the raw stock designated for removal during machining. One machine tool will be used to fabricate the design in Figure 1A, and moves axially in the direction **a**.

Figure 1C illustrates the result of executing a machining operation on the raw stock in Figure 1A in an attempt to create the design shown in Figure 1B using the depicted machine tool. It is clear that a disparity exists between Figure 1B, the original design, and Figure 1C, the fabricated part. Part of the raw stock designated for removal still exists in the remaining stock in Figure 1C. The difference between the remaining stock and the original design is shown in Figure 1D as the inaccessible volume. This is the volume of material in the raw stock that is designated for removal but is inaccessible

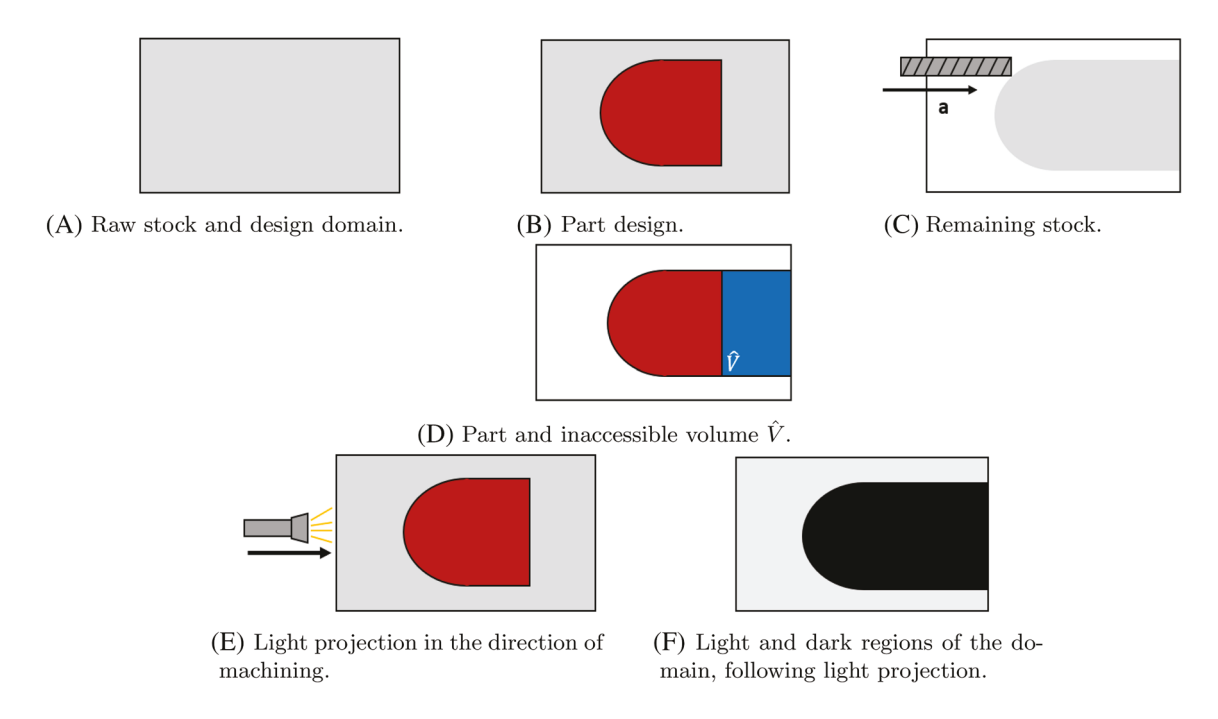


FIGURE 1 Inaccessible volume and its evaluation through light projection

to a machine tool because, in order to access it, the tool would need to translate through a solid feature. It is clear that the presence of any inaccessible volume renders a design non-manufacturable.

Separately, in Figure 1E, light is projected through the domain in the direction of machining, **a**, to differentiate between accessible and inaccessible volumes. Figure 1F illustrates the result of this light projection which yields two volumes, one shaded and one illuminated. The shaded volume is the union of the part design and the inaccessible void volume, as shown in Figure 1D.

A few remarks are merited from comprehensively reviewing Figure 1. First, the existence of a finite, non-zero inaccessible volume in Figure 1D suggests that the physical design is not manufacturable under the present manufacturing specifications (i.e., the number of axes, one, and the orientation of this single axis). This statement is valid because, as was previously established, a manufacturable design is one in which all void regions are accessible to at least one tool. The presence of a solid volume of material in the realized design that corresponds to a void volume in the physical density indicates that this condition has not been fulfilled.

Second, inspecting Figure 1F in the context of Figure 1C clarifies the physical significance of the illuminated and shaded volumes in the former figure. Any material that the machine tool successfully removed to obtain Figure 1C is illuminated in Figure 1F. Thus, the physical interpretation of the illuminated volume resulting from a projection of light into the physical density domain in the direction of the machining is the portion of the domain that can be accessed by a tool piece without passing through a solid geometric feature. This statement also introduces the core motivation for applying an alternative physical model for the evaluation of the machinability of a geometric design. It was concluded previously that the geometric design in Figure 1B is not manufacturable as the inaccessible volume associated with the physical density under the manufacturing conditions, evaluated through a comparison of the nominal and realized designs, was nonzero. Since the shaded volume in Figure 1F is identical to the fabricated design in Figure 1C, it is equally valid to assess the manufacturability of the design by comparing the shaded volume in Figure 1F to the design. It can be visually confirmed that one would obtain the same volume in terms of quantity and spatial distribution by subtracting the physical density from the realized design and the physical density from the shaded volume.

In summary, the presence of inaccessible volume in a domain indicates that the design is not machinable as there exists some volume in the raw stock that has been designated for removal but that is inaccessible to a given set of machine tools. Figure 1 illustrated that evaluating the inaccessible volume in a design can be accomplished by comparing the solid portion of a nominal and realized design. Additionally, projecting light through a design domain in the direction of a machine tool illuminates all regions that are directly accessible to the machine tool, and leaves shaded all volumes in the domain that would be present in the realized design. Thus, it suffices to compare either the solid realized geometry or the shaded portion of the result of light projection through the design domain with the physical density to determine whether an inaccessible volume exists in the physical density which would prevent its realization. For a physical density that contains zero inaccessible volume, all void regions of the design are accessible to at least one tool, and thus the manufacturing of the design via machining is possible. Constraining the quantity of inaccessible volume in a design is therefore a useful metric for ensuring the machinability of a geometric design.

2.1.1 | PDE filtering and Heaviside projection

Prior to introducing a mathematical formulation for inaccessible volume for density-based TO, we first briefly describe the filtering used in this article to the density design field γ . To identify optimal tool orientations and an optimal density distribution, a three-field SIMP density-based topology optimization is implemented.²⁸ Here, $\tilde{\gamma}$ represents the density design variable field γ after PDE filtering.^{29,30} The isotropic PDE filter is given as:

$$-f_R^2 \nabla^2 \tilde{\gamma} + \tilde{\gamma} = \gamma. \tag{1}$$

In Equation (1), f_R is the size of the integral kernel, γ is the density design variable field, and $\tilde{\gamma}$ is the filtered density. f_R is $2\sqrt{3}$ times the filter size in typical density filtering.³⁰

The use of a simple Heaviside projections supports the achievement of a sharpened 0–1 density field. ³¹⁻³³ Equation (2) shows the expression for Heaviside projection used throughout this article:

$$H(\square) = \frac{1}{1 + e^{-2\beta(\square - \eta)}}. (2)$$

Using the filtered density $\tilde{\gamma}$ as the argument in Equation (2) yields the physical density $\overline{\tilde{\gamma}}$. In Equation (2), β controls the sharpness of the transition between 0 and 1 positioned at η . Values less than η are pushed towards zero, and values greater than η are pushed towards unity, resulting in a 0–1 distribution.

2.1.2 | Mathematical formulation of inaccessible volume

We next present the mathematical formulation of an advection-diffused equation interpreted in this article as light projection. Using this equation, a quantitative definition for the inaccessible volume is formed for a general geometric design under some subtractive manufacturing specifications, which includes the number of machine tools and the orientations of the tools present for realization. The strong form of the advection-diffusion equation used to model light projection is as follows:

$$-L^{2}\nabla\cdot(\mathbf{A}\ \nabla\psi)+L\mathbf{v}\cdot\nabla\psi=\beta_{\psi}\hat{\tilde{\gamma}}(1-\psi),\tag{3a}$$

$$\begin{cases} \psi = 0, & x \in \Gamma_D, \{\Gamma_D : \Gamma_D \subset \Gamma, \mathbf{n} \cdot \mathbf{a} \le 0\}, \\ \nabla \psi \cdot \mathbf{n} = 0, & x \in \Gamma_N, \{\Gamma_N : \Gamma \setminus \Gamma_D\}. \end{cases}$$
(3b)

Here, L is the length of the domain in the direction of advection, \mathbf{A} is the diffusion matrix, and \mathbf{v} is the advection term and is oriented in the same direction as the machining orientation \mathbf{a} . Additionally, β_{ψ} is the source magnitude term, $\hat{\bar{\gamma}}$ is a reprojection of the physical density, and ψ is the advection-diffusion solution field, which will also be referred to as the light intensity distribution. Γ is the design domain boundary, \mathbf{n} is the design domain boundary normal.

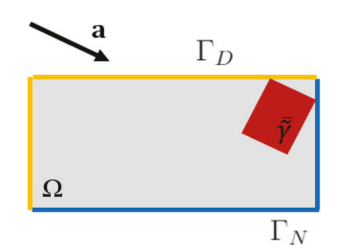
Figure 2 serves to aid in the visualization of some of the terms in Equations (3a) and (3b).

In Figure 2A, an example domain and orientation of machining \mathbf{a} are shown to demonstrate the demarcation of boundaries for the advection-diffusion equation. On Γ_D , $\mathbf{a} \cdot \mathbf{n} \leq 0$. Physically, Γ_D corresponds to all boundaries on which the tool would be considered to be "entering" the domain. ψ is fixed to be zero on Γ_D because ψ accumulates over the domain in the direction of advection (equally, the direction of machining) following a solid geometric feature. With respect to the light projection interpretation of the advection-diffusion equation, fixing ψ to be zero on Γ_D allows the light ($\psi = 0$) to transition to the darkness ($\psi = 1$) following a solid feature in the physical density in the direction of projection. In Figure 2B, illustrations of the terms L, \mathbf{v} , and ψ are shown. Here it is visually shown that L is the length of the domain in the direction of advection, and advection occurs in the same direction as machining (\mathbf{a} and \mathbf{v} are aligned). It can also be seen from Figure 2B that $\psi = 0$ in accessible parts of the domain to the tool, and transitions to $\psi = 1$ following the occurrence of a solid geometric feature in the direction of advection.

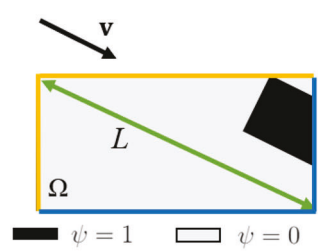
The introduction of the physical model of advection-diffusion enables the numerical identification of inaccessible volume, \hat{V} , for a geometric design. Equation (4) expresses the formal definition for inaccessible volume,

$$\hat{V} = \int_{\Omega} H(\psi - \hat{\tilde{\gamma}}) \ d\Omega. \tag{4}$$

In Equation (4), the integrand of the inaccessible volume consists of a Heaviside projection, H(), of the subtraction of a reprojection of the physical density (a projection of $\overline{\tilde{\gamma}}$ to $\hat{\overline{\tilde{\gamma}}}$) from the advection-diffusion solution field. The reprojection of



(A) Boundary condition definitions for machining axis a.



(B) Distribution of ψ resulting from advection in the direction of \mathbf{v} .

physical density ensures intermediate density in $\overline{\tilde{\gamma}}$ is properly counted in inaccessible volume evaluation. Its effect will be elaborated on subsequently (in Figure 4). Figure 3 visualizes, through an example, each subcomponent of the integrand of the inaccessible volume in Equation (4).

In Figure 3A, a physical density $\bar{\gamma}$ and machining axis **a** are presented. Following a reprojection of the physical density, the advection-diffusion equation introduced in Equation (3) is solved to create Figure 3B, with advection occurring in the same direction as machining **a**.

In Figure 3C, $\hat{\tilde{\gamma}}$ is subtracted from the advection-diffusion solution field, such that only void volumes in the physical density remain in the distribution. In Figure 3D, a Heaviside projection of the field in Figure 3C is shown. The distribution in Figure 3D approaches unity in void volumes of the physical density that are not accessible to a tool, and disappears elsewhere. The integration of the integrand in Equation (4) leads to the volume of the inaccessible region. Since inaccessible volume exists in Figure 3D, the design is not manufacturable.

To facilitate a discussion on the reprojection of the physical density $\overline{\tilde{\gamma}}$ to $\hat{\overline{\tilde{\gamma}}}$ and to better understand its motivation, Figure 4 was created. In Figures 4A–D, the inaccessible void of a design with an internal region of intermediate density is identified without any reprojection of the density itself. That is, to create Figures 4A–D, in both Equations (3) and (4), $\overline{\tilde{\gamma}}$ is substituted for $\hat{\tilde{\gamma}}$. In Figures 4E–H, the advection-diffusion solution field and the inaccessible volume constraints are evaluated as shown in Equations (3) and (4), and use a reprojected density $\hat{\tilde{\gamma}}$.

In Figure 4A, a circular geometry that has intermediate density on its interior is shown. Note the intermediate density is $\overline{\tilde{\gamma}} = 0.6$, while other solid regions are $\overline{\tilde{\gamma}} = 1.0$.

In Figure 4B, the advection-diffusion equation is solved for using the nominal physical density $\overline{\tilde{\gamma}}$ as a source term rather than a reprojected density. The physical density is then subtracted from the advection-diffusion field in Figure 4B to obtain Figure 4C. Figure 4D projects this field, identifying what would be the inaccessible volume integrand of the geometry shown in Figure 4A if no reprojection of the physical density occurred. Note the intermediate density in Figure 4A has not been identified as inaccessible volume in Figure 4D. From the perspective of an inaccessible volume constraint definition, the internal intermediate density volume is classified as solid and thus is not part of an inaccessible volume.

In contrast, to obtain Figure 4E, a Heaviside projection of the density in Figure 4A occurs, using $\eta=0.75$, $\beta=10$ to produce $\hat{\bar{\gamma}}$. Following this reprojection, the internal intermediate density becomes zero in the projected field, resulting in a "hollow" center of the original circular geometry in Figure 4A. While the ψ field is visually indistinguishable between Figure 4B,F, Figure 4G,H differ relatively significantly from Figure 4C,D. The subtraction of the reprojected geometry in Figure 4E from the ψ field in Figure 4F and the subsequent Heaviside projection used to obtain the distribution shown in Figure 4H identify the central, intermediate density of the physical density as inaccessible void (i.e., non-manufacturable).

The reprojection of the physical density is a numerical mechanism which is used here to control intermediate density regions in the evolving density by identifying them as non-manufacturable internal voids. By incrementing the η

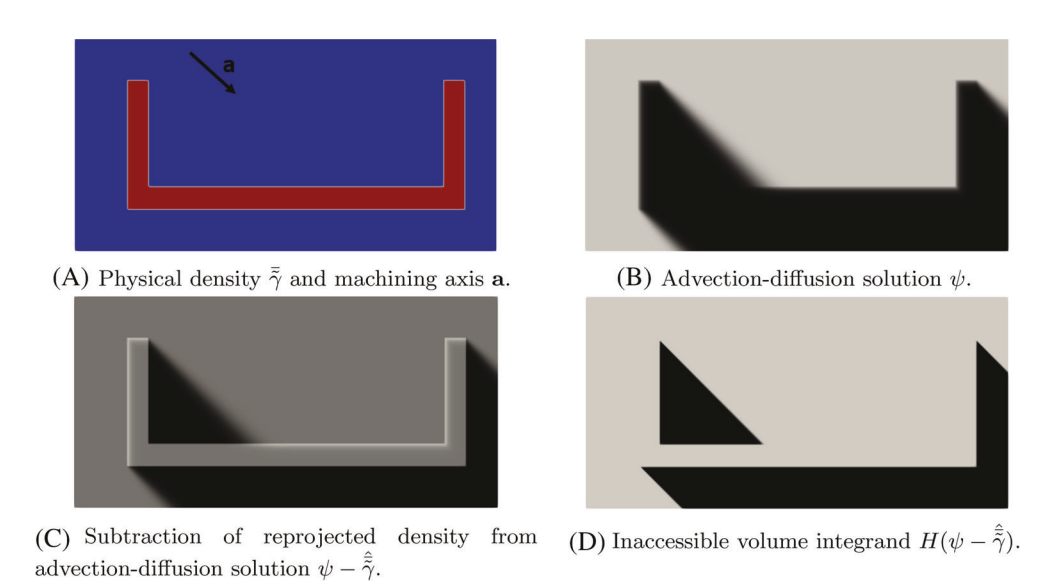


FIGURE 3 Evaluating inaccessible volume for a physical density

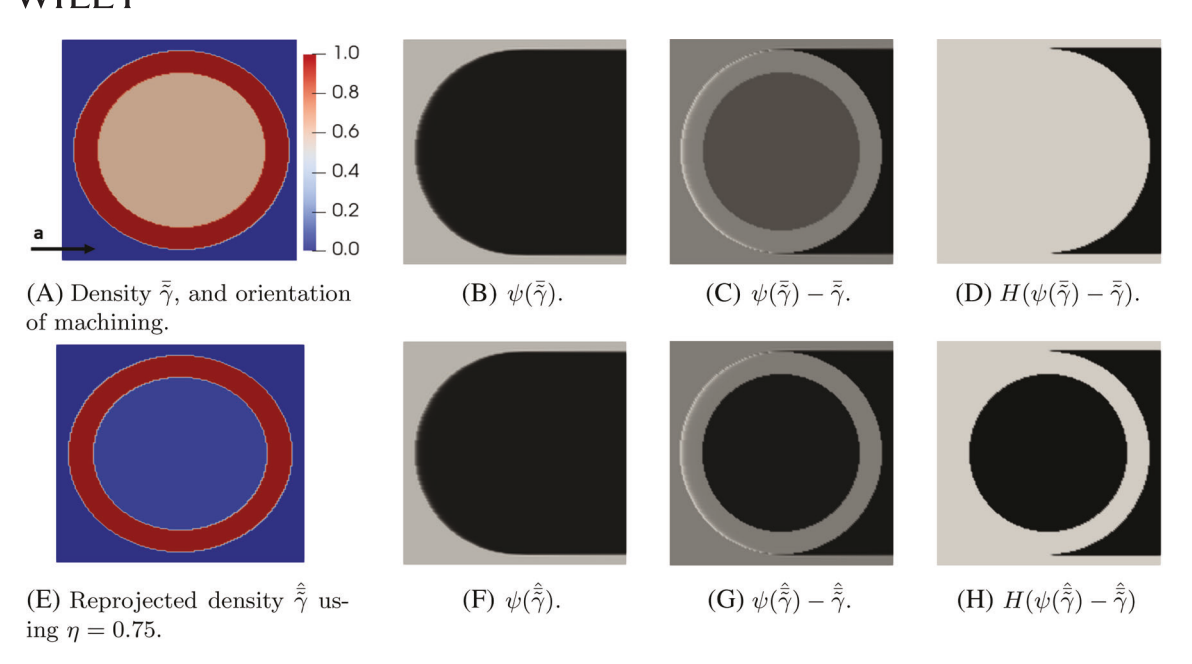


FIGURE 4 Inaccessible volume integrand with and without reprojection

value used to reproject $\overline{\tilde{\gamma}}$ to $\hat{\overline{\tilde{\gamma}}}$, intermediate density regions are gradually forced from the inside of the geometry as they become identified as inaccessible to all machine tools and thus exist in violation of the inaccessible volume constraint. The reprojection of the physical density to $\hat{\overline{\gamma}}$ can be viewed as acting in concert with the SIMP scheme, grayness constraint, and the nominal density Heaviside ($\tilde{\gamma}$ to $\bar{\tilde{\gamma}}$) to obviate intermediate density regions. This additional method is pertinent as it was empirically observed that relatively small, internal intermediate density regions tended to form during optimization. These regions were sufficiently small such that did not violate the global grayness constraint and were not eliminated by the other aforementioned numerical schemes. A distinct Heaviside reprojection for use in manufacturability analysis allows for the free manipulation of η to obtain $\hat{\tilde{\gamma}}$, whereas incrementing the η associated with obtaining $\tilde{\gamma}$ analogously may have wider implications for the convergence of other constraints and the optimization in general. Given this additional Heaviside reprojection of the physical density does not significantly complicate the scheme nor increase the computational cost, it is justifiable as a tool for eliminating intermediate grayness.

We now introduce a multi-axis definition for the global inaccessible volume. Equation (5) introduces this as the simple intersection of the inaccessible volumes specific to an orientation of machining:

$$\hat{V} = \int_{\Omega} \prod_{i} H(\psi_{i} - \hat{\tilde{\gamma}}) d\Omega.$$
 (5)

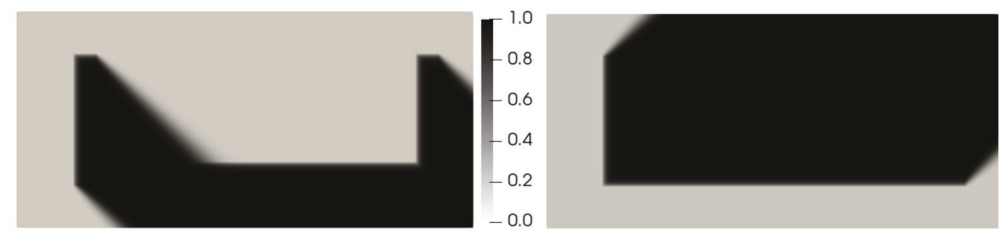
In Equation (5), the term ψ_i denotes the advection-diffusion distribution specific to a given orientation of machining, \mathbf{a}_i . To illustrate the formation of the integrand in Equation (5), Figure 5 has been included. Figure 5 uses the same physical density as was shown in Figure 3, and incorporates two axes, \mathbf{a}_1 and \mathbf{a}_2 , into the attempted manufacturing of the design.

In Figure 5B–D, the same process as was used in Figure 3 is executed on a machine-axis specific basis. That is, the advection-diffusion solution fields and subsequent inaccessible volumes identified in Figure 5D \hat{V}_1 and \hat{V}_2 are specific to either \mathbf{a}_1 or \mathbf{a}_2 . With a second machine axis present, the only additional step required to identify the (global) inaccessible volume is to intersect the inaccessible volumes common to all machine tools. This operation is performed in Figure 5E, elucidating the void region of the physical density that cannot be accessed by either a tool moving along \mathbf{a}_1 or \mathbf{a}_2 due to occluding solid regions of the design. As was true for the single-axis case presented in Figure 3, the presence of a finite, non-zero inaccessible volume indicates the design is not manufacturable. As the global inaccessible volume disappears, all material in the original stock workpiece designated for removal become accessible to at least one tool piece translating in a specified direction.

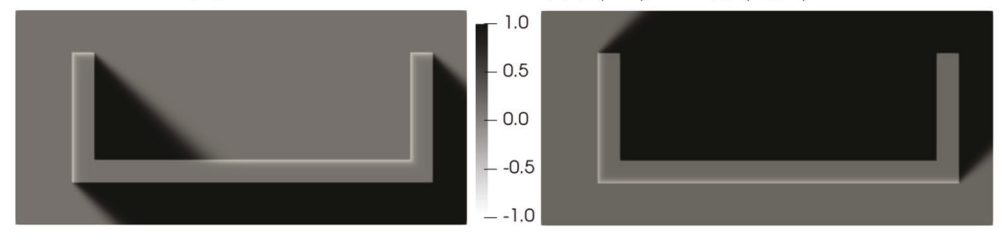
Following the introduction of multi-axis inaccessible volume, the motivation for the outer Heaviside projection in Equations (4) and (5), $H(\psi - \hat{\tilde{\gamma}})$, becomes more obvious. Using a more complex geometry, Figure 6 facilitates this



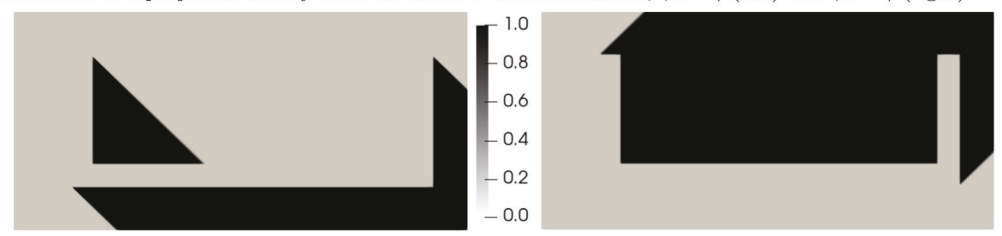
(A) Physical density and orientations of machining, \mathbf{a}_1 and \mathbf{a}_2 .



(B) Advection-diffusion solutions, ψ_1 (left) and ψ_2 (right).



(C) Subtraction of reprojected density from advection-diffusion solutions, $\psi_1 - \hat{\bar{\gamma}}$ (left) and $\psi_2 - \hat{\bar{\gamma}}$ (right).



(D) Integrand of machine axis-specific inaccessible volume, \hat{V}_1 (left) and \hat{V}_2 (right).



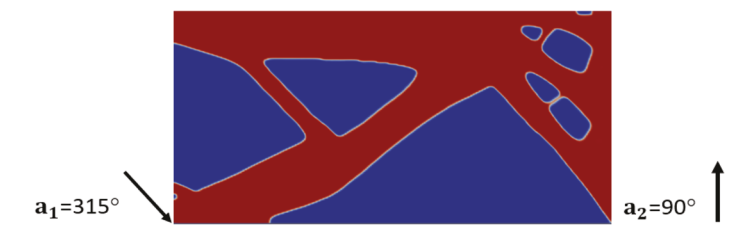
(E) Integrand of global inaccessible volume, \widehat{V} .

FIGURE 5 Evaluating global inaccessible volume for multi-axis machining (Example 1)

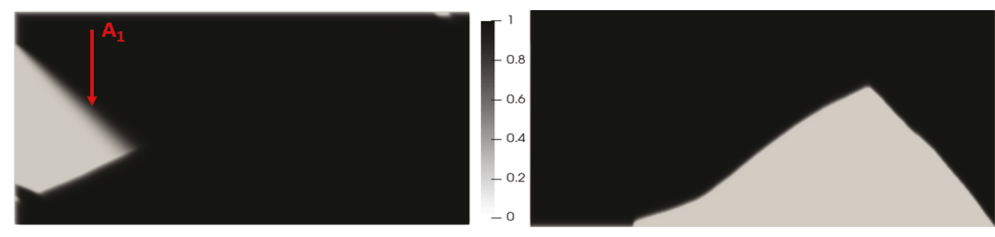
discussion and performs analogous operations as were shown in Figure 6 using two new orientations for the machine axes \mathbf{a}_1 and \mathbf{a}_2 .

A Heaviside projection of the field $\psi - \hat{\tilde{\gamma}}$ addresses three potential sources of concern simultaneously by: (1) yielding a distribution that is [0,1], rather than approximately [0,1], (2) practically eliminating the possibility of the intersection of inaccessible volumes disappearing, (3) ensuring a sharp transition between inaccessible volumes and adjacent volumes.

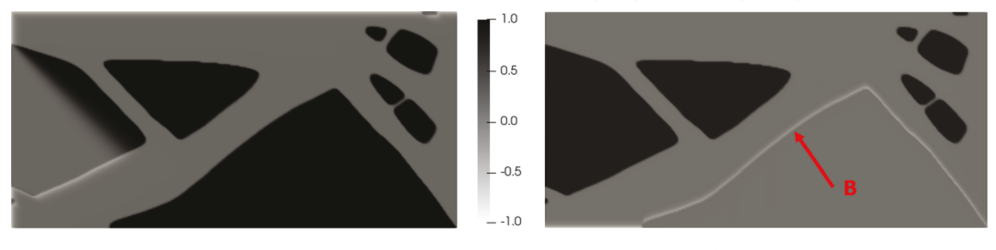
The first point is relevant with respect to Figure 6B (and similarly, Figure 5B). While these fields have been plotted as [0,1] for clarity and discussion purposes, the ψ field is approximately [0,1] rather than the ideal [0,1] due to minor oscillations in the numerical solution. This behavior is symptomatic of the advection-dominated nature of



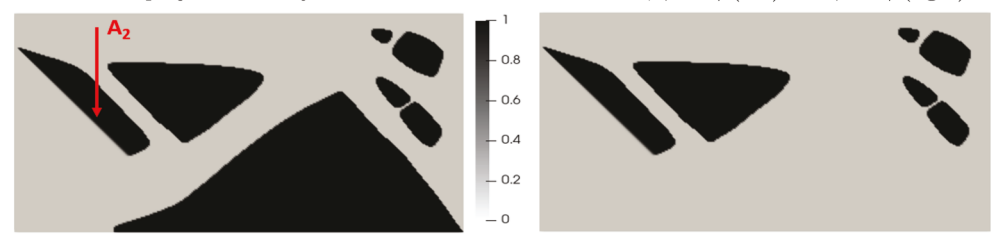
(A) Physical density, and orientations of machining, \mathbf{a}_1 and \mathbf{a}_2 .



(B) Advection-diffusion solutions, ψ_1 (left) and ψ_2 (right).



(C) Subtraction of reprojected density from advection-diffusion solutions, $\psi_1 - \hat{\tilde{\gamma}}$ (left) and $\psi_2 - \hat{\tilde{\gamma}}$ (right).



(D) Integrand of inaccessible volume, \widehat{V}_1 (left) and \widehat{V}_2 (right).



(E) Integrand of global inaccessible volume, \widehat{V} .

FIGURE 6 Evaluating global inaccessible volume (Example 2)

the advection-diffusion equation, but implies that the ψ field may approach unity rather than exactly attain unity in visually shaded volumes of the domain. As was shown in Figure 6, extending Equation (4) to encompass cases of multiple axes requires the simple intersection of machine tool-specific inaccessible volumes. To directly intersect quantities that approach but do not equal unity over an unknown number of axes introduces the possibility of the final intersected value disappearing (i.e., even for a small but finite ϵ , $\lim_{n\to\infty} (1-\epsilon)^n = 0$). By projecting each $\psi_i - \hat{\gamma}$ field, the possibility of the intersection of these fields disappearing over an arbitrary number of axes practically vanishes.

Second, the subtraction of the reprojected density is the numerical implementation of the idealized identification of the inaccessible volume in Figure 1D, which occurs through the subtraction of the physical density in Figure 1B from

the realized structure in Figure 1D. As was discussed previously, this could be equally evaluated as the subtraction of the physical density in Figure 1B from the shaded volume in Figure 1F. In Figure 1, this subtraction precisely elucidated the inaccessible volume. In Figure 6, this is not necessarily true, as the distribution in Figure 6C is no longer approximately [0,1], but rather is approximately [-1,1]. This phenomena can be ascribed to the numerical solution to 1, which leads to a ψ that transitions, rather than steps, between 0 and 1 when a solid geometric feature is encountered in the direction of advection or light projection. For a sharp solid geometry such as the one shown in Figure 6A, $\hat{\tilde{\gamma}}$ transitions from void to solid in the direction of advection sufficiently quickly such that in the solution field $\psi < \hat{\tilde{\gamma}}$. This leads to negative values spatially located on the solid/void interface of the physical density. One example of this is illustrated in Figure 6C at B. These negative values are of potential concern as the domain integration of $\psi - \frac{\hat{\tau}}{\tilde{\gamma}}$ would be an efficient mechanism for assessment of inaccessible volume, but becomes physically meaningless and may lead to incorrect conclusions about the manufacturability of a physical density if negative values and positive values are included in the integral. Integrating the distribution in Figure 6C directly would allow for non-machinable features to form if other arbitrary geometric patterns were present in the physical density as a cancellation between positive and negative values would occur during the subsequent integration.

Third, although numerical parameters for Equation (3) have been selected such that the advection-diffusion equation is advection-dominated, in Figure 6B, near the light-dark boundary annotated as A_1 , a somewhat diffuse transition between light and dark is observable. Direct integration of this may lead to an overidentification of occluded, shaded volume in the domain. Sharpening this transition to be more nearly zero in all accessible volumes and more nearly unity in all occluded volumes both increases the precision of inaccessible volume evaluation and is more consistent with the physical interpretation of the advection-diffusion equation as a light projection problem.

Following the introduction and discussion of the physical significance and mathematical definition of the inaccessible volume constraint, this constraint can be incorporated into a topology optimization formulation. This formulation allows for the generation of designs that are optimal for some physical loading and are machinable.

3 TOPOLOGY OPTIMIZATION FORMULATION

The developed constraint Equation (5) can be incorporated into a TO procedure to ensure the subtractive manufacturability of the final design. We choose a linear elasticity problem for numerical experimentation, and so we minimize the compliance with respect to the optimization variables γ and \mathbf{a}_i .

$$\min_{\gamma, \mathbf{a}_i} \quad J = \int_{\Gamma_t} \mathbf{tu} \, d\Gamma_t \tag{6a}$$

s.t.
$$a(\mathbf{u}, \tilde{\mathbf{u}}) = l(\tilde{\mathbf{u}}), \ \forall \tilde{\mathbf{u}} \in V_0$$
 (6b)

$$\left(\frac{\int_{\Omega} \overline{\tilde{\gamma}} \, d\Omega}{\overline{V_f}}\right)^{p_{vol}} \le 1$$
(6c)

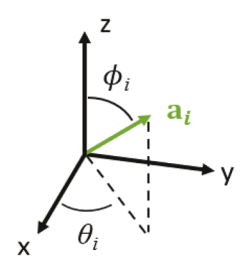
$$\left(\frac{\int_{\Omega} 4\overline{\widetilde{\gamma}}(1-\overline{\widetilde{\gamma}}) d\Omega}{\overline{\epsilon}}\right)^{p_{gray}} \le 1$$
(6d)

$$\left(\frac{\int_{\Omega} 4\overline{\widetilde{\gamma}}(1-\overline{\widetilde{\gamma}}) d\Omega}{\overline{c}}\right)^{p_{gray}} \leq 1$$

$$\frac{\int_{\Omega} \Pi_{i} \left[H(\psi_{i}-\widehat{\overline{\widetilde{\gamma}}})\right] d\Omega}{\overline{\widetilde{V}}} \leq 1.$$
(6d)

In this formulation, Equation (6a) represents the structural compliance, (6b) is the weak form of the state equation for linear elasticity with u, ũ being the displacement field and test functions, respectively. Equation (6c) is an exponential volume fraction constraint, (6d) is an exponential grayness constraint, and (6e) is the subtractive manufacturability constraint. \overline{V}_f , $\overline{\epsilon}$, and $\overline{\hat{V}}$ represent the maximum allowable amount of solid material volume, intermediate density, and inaccessible volume, respectively, in the final design. The exponential formulations of the typical volume and grayness constraints ensure convergence for intrusive applications of the manufacturability constraint by increasing the sensitivity of the constraints with respect to the design variables during optimization. A discussion on the motivation for, and efficacy of, these exponential power terms follows in Section 5 during the discussion of results.





(A) 2D representation of machine axis through θ_i . (B) 3D representation of machine axis through θ_i , ϕ_i .

FIGURE 7 Representation of machine axis in 2D and 3D coordinate systems

In 2D (Equation (7a)) and 3D (Equations (7b)), the orientation of machining can be described as:

$$\mathbf{a}_i = [\cos(\theta_i), \sin(\theta_i)] \quad \theta_i \in [0, 2\pi] \tag{7a}$$

$$\mathbf{a}_i = [\sin(\phi_i)\cos(\theta_i), \sin(\phi_i)\sin(\theta_i), \cos(\phi_i)] \qquad \phi_i \in [0, \pi], \quad \theta_i \in [0, 2\pi]. \tag{7b}$$

Figure 7 shows the representation of a machining axis in 2D and 3D coordinate systems.

When including the orientations of machining \mathbf{a}_i in the optimization as degrees of freedom, the design variables are θ_i in 2D, and in 3D, the design variables per axis are taken as ϕ_i , θ_i , where i represents the ith machining axis.

We apply a SIMP scheme to prevent intermediate density solutions from forming, leading to an interpolation of the Young's modulus $E(\tilde{\gamma}) = E_{min} + (E_0 - E_{min})\tilde{\gamma}^p$. In our work, E_0 is the Young's modulus for a solid material, and $E_{min} = 10^{-9}$ to prevent singularities during finite element analysis. p, the penalization factor, is set to 3. The MMA³⁴ is used to solve the design problem. The sensitivity of the new constraint to the optimization variables are derived in Section 4.

4 | SENSITIVITY ANALYSIS

Here, we derive the sensitivity of the manufacturability constraint with respect to the design variables for use in gradient-based optimization. The sensitivity of the volume constraint and the cost function are well-known in the TO community, and so are not included here. Additionally, the sensitivity for the grayness constraint can be found in detail in Reference 27. Thus, the analysis will include the derivation for the manufacturability constraint with respect to the density and the orientations of machining. Our implementation is through the finite element solver FEniCS, which automatically executes FEA through the weak form of PDEs and as a result these expressions will be presented in their variational forms. In the analysis, $\delta \gamma$ is the variation of the node-based optimization variable γ , with the variation of the density design variables after the application of the Helmholtz filter a Heaviside project represented as $\delta \tilde{\gamma}$, $\delta \tilde{\gamma}$, respectively. The relationships between these variables are obtained from a straightforward differentiation of the isotropic Helmholtz PDE and the density Heaviside projection. In the following expressions, the derivative of the simple Heaviside is shown as $H'(\Box)$ for brevity, and is explicitly $H'(\Box) = \frac{-2\beta e^{-2\beta(\Box-\eta)}}{(1+e^{-2\beta(\Box-\eta)})^2}$.

First, we show the weak form of the advection-diffusion equation specific to a single machine axis \mathbf{a}_i . This is obtained by multiplying the strong form of the governing equation, shown in Equation (3), by a test function $\tilde{\psi}_i$ and integrating over the domain. This leads to Equation (8):

$$\int_{\Omega} \beta_{\psi} \tilde{\psi}_{i} \hat{\tilde{\gamma}} (1 - \psi_{i}) \ d\Omega - \int_{\Omega} L_{i}^{2} \nabla \tilde{\psi}_{i} \cdot \mathbf{A}_{i} \nabla \psi_{i} \ d\Omega - \int_{\Omega} L_{i} \tilde{\psi}_{i} \mathbf{v}_{i} \cdot \nabla \psi_{i} \ d\Omega = 0 \quad \forall \tilde{\psi}_{i} \in V_{0}.$$

$$(8)$$

Following a continuous adjoint approach, we form the Lagrangian \mathcal{L} specific to a machining axis i, which adjoins the manufacturability constraint and the weak form of the advection-diffusion equation. The result is a functional of the state variable ψ_i , the adjoint variable ζ_i , and the physical density,

$$\mathcal{L}_{i} = \int_{\Omega} \prod_{i} [H(\psi_{i} - \hat{\tilde{\gamma}})] d\Omega + \int_{\Omega} \beta_{\psi} \hat{\tilde{\gamma}} (1 - \psi_{i}) \zeta_{i} d\Omega + \int_{\Gamma_{N}} L_{i}^{2} \zeta_{i} (\mathbf{A}_{i} \nabla \psi_{i} \cdot \mathbf{n}) d\Gamma_{N}
- \int_{\Omega} L_{i}^{2} \nabla \zeta_{i} \cdot (\mathbf{A}_{i} \nabla \psi_{i}) d\Omega - \int_{\Omega} L_{i} \mathbf{v}_{i} \cdot \nabla \psi_{i} d\Omega.$$
(9)

The Lagrangian's directional derivative with respect the state variable ψ_i is set equal to zero, yielding the machine axis-specific adjoint equation, that is,

$$\mathcal{L}_{i,\delta\psi_{i}} = 0$$

$$= \int_{\Omega} \prod_{j,j\neq i} [H(\psi_{j} - \hat{\bar{\gamma}})] H'(\psi_{i} - \hat{\bar{\gamma}}) \delta\psi_{i} \, d\Omega - \int_{\Omega} \beta_{\psi} \hat{\bar{\gamma}} \zeta_{i} \delta\psi_{i} \, d\Omega + \int_{\Gamma_{N}} L_{i}^{2} \zeta_{i} (\mathbf{A}_{i} \nabla \delta\psi_{i} \cdot \mathbf{n}) \, d\Gamma_{N}$$

$$- \int_{\Omega} L_{i}^{2} \nabla \zeta_{i} \cdot (\mathbf{A}_{i} \nabla \delta\psi_{i}) \, d\Omega - \int_{\Omega} L_{i} \mathbf{v}_{i} \cdot \nabla \delta\psi_{i} \, d\Omega. \tag{10}$$

An expression for the gradient is obtained by taking the first order variation of the Lagrangian with respect to the density, that is,

$$\mathcal{L}_{i,\delta\overline{\tilde{\gamma}}} = \sum_{i} \left[\int_{\Omega} -\prod_{j,j\neq i} [H(\psi_{j} - \hat{\tilde{\gamma}})] H'(\psi_{i} - \hat{\tilde{\gamma}}) H'(\overline{\tilde{\gamma}}) \delta\overline{\tilde{\gamma}} \ d\Omega + \int_{\Omega} \beta_{\psi} \zeta_{i} (1 - \psi_{i}) H'(\overline{\tilde{\gamma}}) \delta\overline{\tilde{\gamma}} \ d\Omega \right]. \tag{11}$$

The sensitivity for each orientation of machining is found through and analogous first order variation of the Lagrangian with respect to the machining orientation $\delta\Theta_i$, where Θ_i represents the orientation variable(s) present. In 2D, this is θ_i , in 3D this is θ_i or ϕ_i . In the following equations, the sensitivities of L_i , \mathbf{v}_i , and \mathbf{A}_i to the orientation are as L_{i,Θ_i} , \mathbf{v}_{i,Θ_i} , and \mathbf{A}_{i,Θ_i} . Equation (12) explicitly shows this first order variation:

$$\mathcal{L}_{i,\delta\Theta_{i}} = \int_{\Gamma_{N}} 2L_{i}L_{i,\delta\Theta_{i}}\zeta_{i}(\mathbf{A}_{i}\nabla\psi_{i}\cdot\mathbf{n}) d\Gamma_{N} + \int_{\Gamma_{N}} L_{i}^{2}\zeta_{i}(\mathbf{A}_{i,\delta\Theta_{i}}\nabla\psi_{i}\cdot\mathbf{n}) d\Gamma_{N} - \int_{\Omega} 2L_{i}L_{i,\delta\Theta_{i}}\nabla\zeta_{i}\cdot(\mathbf{A}_{i}\nabla\psi_{i}) d\Omega + \int_{\Omega} L_{i}^{2}\nabla\zeta_{i} \\
\cdot (\mathbf{A}_{i,\delta\Theta_{i}}\nabla\psi_{i})d\Omega - \int_{\Omega} L_{i,\Theta_{i}}\zeta_{i}\mathbf{v}_{i}\cdot\nabla\psi_{i} d\Omega - \int_{\Omega} L_{i}\zeta_{i}\mathbf{v}_{i,\delta\Theta_{i}}\cdot\nabla\psi_{i} d\Omega. \tag{12}$$

In 2D (Equation (13a)) and 3D (Equations (13b)–(13c)), the sensitivity of the machine orientation to the design variable Θ_i is shown:

$$\mathbf{a}_{i,\theta} = [-\sin(\theta_i), \cos(\theta_i)] \quad \theta_i \in [0, 2\pi]$$
(13a)

$$\mathbf{a}_{i,\theta} = [-\sin(\phi_i)\sin(\theta_i),\sin(\phi_i)\cos(\theta_i),0] \tag{13b}$$

$$\mathbf{a}_{i,\phi} = [\cos(\phi_i)\cos(\theta_i), \cos(\phi_i)\sin(\theta_i), -\sin(\phi_i)]. \tag{13c}$$

The advection term $\mathbf{v}_i = \overline{v}\mathbf{a}_i$, such that $\mathbf{v}_{i,\Theta_i} = \overline{v}\mathbf{a}_{i,\Theta_i}$. The length of the domain in the direction of machining is defined as $L_i = ((L_x \cos(\theta_i))^2 + (L_y \sin(\theta_i))^2)^{1/2}$ in 2D where L_x , L_y are the dimensions of the domain in the x- and y-directions. This makes $L_{i,\Theta_i} = L_i^{-1/2} \cos(\theta_i) \sin(\theta_i) (-L_x^2 + L_y^2)$ in 2D.

The diffusion tensor A_i is defined in 2D as:

$$\mathbf{A}_{i} = \begin{bmatrix} \epsilon + (\cos^{2}(\theta_{i}))^{1/2} & 0\\ 0 & \epsilon + (\sin^{2}(\theta_{i}))^{1/2} \end{bmatrix}. \tag{14}$$

The square and square root are a 2-step, numerical, differentiable manner of taking the absolute value of a quantity, where the square is applied first, then the square root is applied subsequently. In 2D, this makes the sensitivity of the diffusion tensor:

$$\mathbf{A}_{i,\Theta_i} = \cos(\theta_i)\sin(\theta_i) \begin{bmatrix} -(\cos^2(\theta_i))^{-1/2} & 0\\ 0 & (\sin^2(\theta_i))^{-1/2} \end{bmatrix}.$$
 (15)

Similarly here, the exponential operations are carried out sequentially. The definitions and sensitivities of the domain length L_i and diffusion tensor \mathbf{A}_i in 3D follow directly from their 2D counterparts, and so are omitted.

An important detail surfaces here. In Section 2, the boundary conditions for the advection diffusion PDE were presented such that the boundaries themselves were a function of the orientation of machining, that is, $\Gamma_D = \Gamma_D(\mathbf{a})$, and

 $\Gamma_N = \Gamma_N(\mathbf{a})$. The above sensitivity analysis does not explicitly consider the sensitivity of the boundaries to a perturbation in the orientation of machining. It was found that this was a justifiable simplification through a comparison of two sets of results. The first of these was obtained using the proposed boundary conditions and the above sensitivities, and the second used a set of relatively computationally inefficient but static (i.e., Γ_D , Γ_N were constant) boundary conditions, which ensured differentiability. The results were found to be sufficiently comparable and thus the originally proposed boundary conditions were used. For a more thorough discussion on this comparison, refer to Appendix A.

5 | NUMERICAL IMPLEMENTATION AND EXAMPLES

In this section, we first motivate the use and discuss the utility of exponential power terms placed on the typical volume and grayness constraints. Next, we present our numerical scheme and numerical results for subtractive manufacturability constrained optimized geometries in 2D (Section 5.2) and 3D (Section 5.3).

5.1 | Exponential volume and gray constraints

In Equations (6c) and (6d), nominal volume and grayness constraints are raised to exponential powers, p_{vol} and p_{gray} , respectively. The motivation for amending these constraints is better understood by first exploring the challenges to TO posed by incorporating the proposed manufacturability constraint into a 3-constraint optimization. Qualitatively, it is expected that a relatively aggressive level of control must be achieved over inaccessible volumes because any finite inaccessible void renders the entire geometry non-manufacturable to machine tools moving with their specified orientations. To achieve this, the inaccessible volume was generally constrained to be arbitrarily low and was enforced rapidly and immediately during optimization. This adversely affected the convergence of the volume and grayness constraints as the subsequent achievement of specified values of \overline{V}_f and $\overline{\epsilon}$ required relatively steep, sometimes insurmountable increases in cost or an impractically extended number of iterations. Exponential terms were used to simultaneously overcome this scaling issue and to more rapidly achieve convergence by preventing significant initial divergence of the volume and grayness constraints.

To illustrate the challenge of simultaneously achieving Equations (6c)–(6e) and how this varies as a function of the level of allowed inaccessible volume \hat{V} , consider Figure 8. In this figure, the sum-of-squares total constraint violation of the volume and grayness is displayed over the first 100 iterations of an optimization for different allowed inaccessible volume \hat{V} . Explicitly, the value plotted on the ordinate of Figures 8,9A,C is shown in Equation (16) as S:

$$S = \frac{1}{\sqrt{2}} \sqrt{\left(\frac{V_f}{\overline{V}_f}\right)^2 + \left(\frac{\epsilon}{\overline{\epsilon}}\right)^2}.$$
 (16)

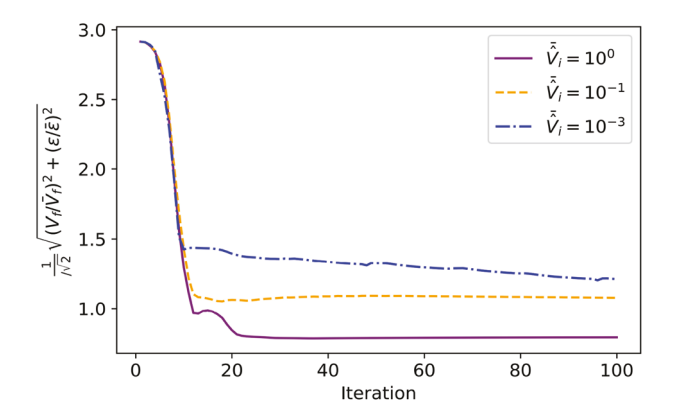


FIGURE 8 Violation for different allowed inaccessible volume \hat{V}

1.4 1.2

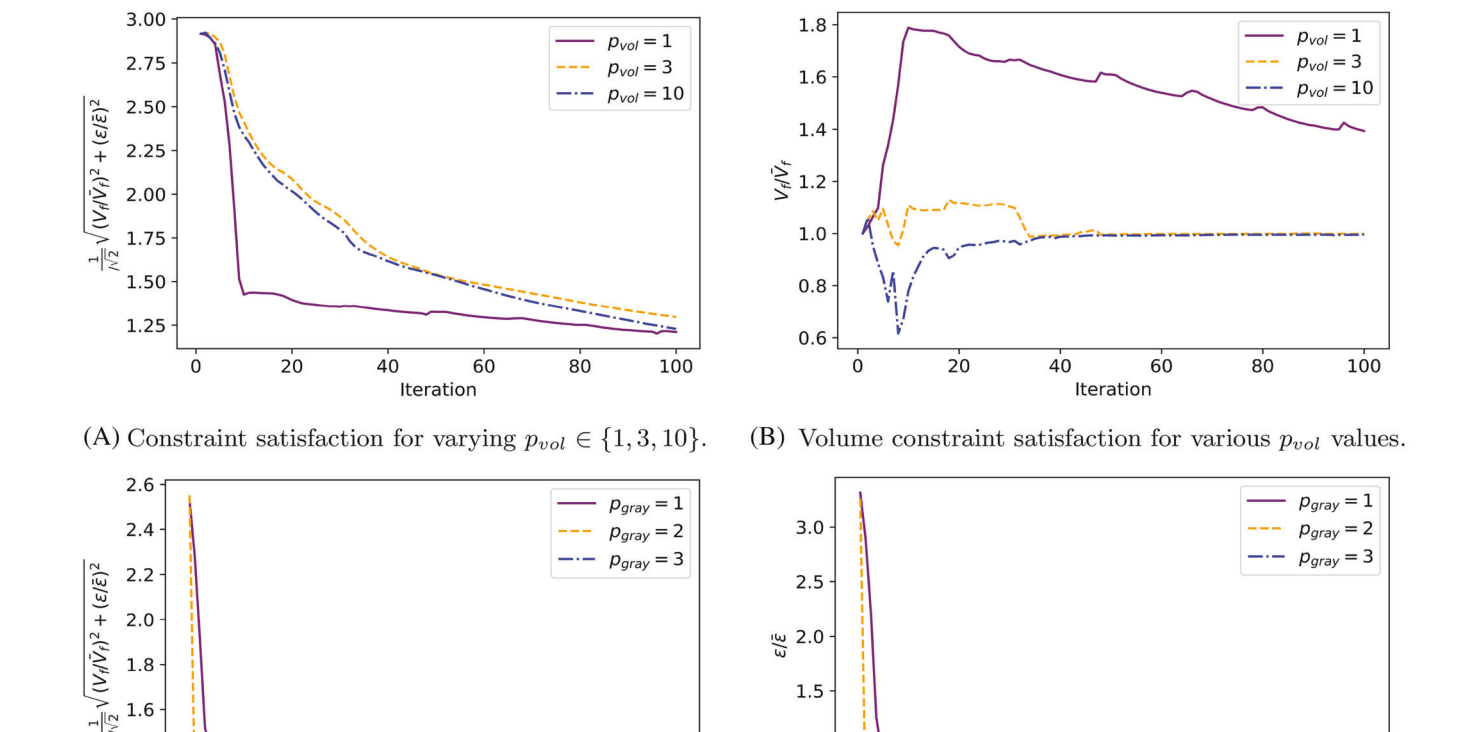
20

40

For an optimization in which the grayness and volume constraints have been perfectly satisfied (e.g., $V_f = \overline{V}_f$) or are inactive, S will be less than or equal to unity. For any instance in which S is greater than unity, at least one constraint has been violated. It is self-evident that these statements are independent of the values of \underline{p}_{vol} and \underline{p}_{gray} . All optimizations in Section 5.1 are simplified, single-, fixed-axis optimizations for $\mathbf{a}=45^\circ$, with $\overline{\epsilon}=0.25$, $\overline{V}_f=0.5$, and the initial density set to \overline{V}_f everywhere. A continuation scheme is placed only on $\overline{\hat{V}}$, which is decreased by 50% every 15 iterations from $10\times$ its final value. This reduced-complexity numerical scheme compared to the actual numerical scheme introduced in Section 5.2 is designed to elucidate the effects of the exponential constraints. In Figure 8, the value of $\overline{\hat{V}}$ displayed in the legend is the final value of this parameter at the end of the continuation scheme. For the case with $\overline{\hat{V}}=10^{-1}$, a maximum of 10% of the domain volume can be inaccessible void.

Figure 8 reinforces the concept that there is inherent difficulty in achieving the three constraints in Equations (6c)–(6e) due to the extent of \hat{V} control. The value $\overline{\hat{V}}=10^{-3}$ is representative of the level of \hat{V} control sought during the optimizations used to create numerical results. From Figure 8, it is evident that, all other parameters being equal, the enforcement of the manufacturability constraint on the level that is required to practically eliminate inaccessible volume from the domain significantly prolongs convergence. When the allowed inaccessible volume $\overline{\hat{V}}=10^0$, the constraint is inactive, and the combined grayness and volume constraints are less than unity. Increasing the restrictiveness of $\overline{\hat{V}}$ by an order of magnitude results in a sum-of-squares of constraint violation that is greater than one, signifying at least one of the two constraints is being violated. Further, there is no clear indication that even an extended number of iterations will be sufficient for achieving convergence.

To address this, the volume and grayness constraints can be raised to exponential powers. Depending on the magnitude of the power value, this scheme is useful for enforcing ongoing adherence to the constraint target values \overline{V}_f and $\overline{\epsilon}$. Effectively, this scheme results in an increased cost during the initial iterations of an optimization but achieves immediate constraint convergence. A series of four plots shown collectively as Figure 9 depict the type of analysis performed to select



(C) Constraint satisfaction for varying $p_{gray} \in \{1, 2, 3\}$. (D) Grayness constraint satisfaction for various p_{gray} values.

100

1.0

0.5

20

40

60

Iteration

80

100

FIGURE 9 Constraint satisfaction under varying exponential parameters p_{vol} and g_{grav}

60 Iteration 80

these values for the case in Figure 6 corresponding to $\widehat{V}=10^{-3}$. Figure 9A,C show the sum-of-squares constraint satisfaction for increasing exponential terms on either the volume or the grayness constraint, while the other exponential term is held constant. In Figure 9B,D, the constraint satisfaction particular to the exponentially weighted term is plotted over the first 100 iterations of the optimization. Note, for clarity, the first five iterations have been omitted from Figure 9C,D due to relatively large initial values which result from a completely gray initial density distribution and thus a large constraint violation.

Reviewing Figure 9B evidences that increasing p_{vol} to 10 yields near-total adherence to the volume fraction throughout the first 100 iterations, contrasting the volume fraction behavior under the nominal $p_{vol} = 1$. However, Figure 9A indicates the overall constraint violation has decreased, a manifestation of complete volume fraction satisfaction at the cost of non-convergent grayness.

Figure 9D contrasts Figure 9B in that for $p_{gray}=1$, grayness constraint satisfaction is complete whereas the volume constraint is consistently violated under $p_{vol}=1$. However, increasing p_{gray} has implications for the grayness constraint during the optimization. For increased p_{gray} values, decrements in $\overline{\hat{V}}$ lead to minor perturbations in the grayness constraint as the geometric design is forced to meet a tightened manufacturability constraint and is obstructed from meaningfully increasing grayness beyond the selected threshold to achieve this. Figure 9C also illustrates that increasing p_{gray} is shown to increase volume fraction deviation, as it can be seen from Figure 9D that $\epsilon \leq \overline{\epsilon}$ but the sum-of-squares constraint violation in Figure 9C increases for increasing p_{gray} .

A concise summary of Figure 9 is that the exponential terms in Equations (6c) and (6d) form a weighting scheme and that arbitrarily increasing the exponent on a constraint leads to complete, and potentially immediate, convergence for a given constraint. However, this can cause other constraints to diverge, as the optimization becomes relatively sensitive to a single constraint. Simple empirical experimentation leads to the single-axis set of values for p_{vol} , p_{gray} , which promotes simultaneous constraint convergence. A comparison between some sample schemes are shown in Figure 10.

In 2D, for all single and multiple fixed-axis experiments $p_{gray} = 2$ initially. For the former and latter optimizations, initially $p_{vol} = 25$ and $p_{vol} = 15$, respectively. For variable-axis $p_{vol} = 5$, $p_{gray} = 2$ is used. In recognition of the potentially over-restrictive and highly nonlinear nature of these constraints, p_{vol} is decremented starting at iteration 150 for fixed, single-axis optimization or iteration 100 in all other optimizations every 10 iterations by one if the volume constraint is met.

In 3D, the satisfaction of all constraints was more organic. For fixed axis experimentation, $p_{vol} = 20$ and $p_{gray} = 2$. For variable axis experimentation, $p_{vol} = 5$, and $p_{gray} = 2$.

5.2 | 2D numerical implementation and results

This section presents a series of 2D results for a minimal compliance design problem as evidence of the efficacy of the inaccessible volume-based manufacturability constraint in a simplified setting. All optimizations use a Poisson's ratio of

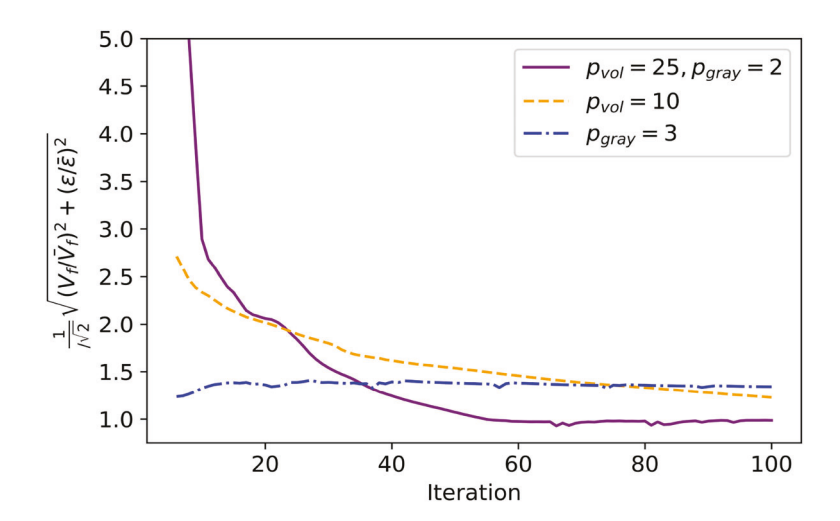


FIGURE 10 Volume, grayness constraint satisfaction under varying numerical schemes for p_{vol} , p_{gray}

v = 0.3, and a volume fraction of $V_f = 0.5$. The Helmholtz PDE density filter used a filter radius $f_R = 5/(2\sqrt{3}h)$, with h being the elemental length.

The cost was normalized at iteration 1 in all optimizations to prevent scaling issues.³⁴ When discussing all subsequent results, "fixed-axis" optimization refers to optimizations in which minimization occurred with respect to the density design variables and not the orientation of machining, as the latter has been "fixed" or pre-oriented. Optimizations introduced as "variable-axis" optimizations minimize compliance with respect to both the density and the orientation(s) of machining, as the orientation(s) develop ("vary") over the course of the optimization. Determining a uniform termination criteria for all optimizations was complicated by the exponential power terms, which led to numerous cases of premature termination or no termination at all due to ongoing changes in density at certain points. For 2D problems, single axis fixed-axis and variable-axis optimizations were assumed to require 200 or 225 iterations, respectively, and were conferred additional iterations if convergence was not complete. Multi-axis optimizations were uniformly given 150 iterations to converge.

The following parameters apply uniformly for 2D experimentation unless otherwise noted. In Equation (3), $\bar{\nu}=10^3$, $\beta_{\psi}=100\bar{\nu}$. Single axis optimizations invoked a density Heaviside (i.e., the projection of $\tilde{\gamma}$ to $\tilde{\tilde{\gamma}}$) at iteration 40, all other 2D optimizations did similarly at iteration 20. In both scenarios the initial β was set to 5, and incrementation occurred every 20 iterations. The reprojection of the density through a Heaviside for manufacturability constraint evaluation in Equation (5) (i.e., the projection of $\tilde{\gamma}$ to $\hat{\tilde{\gamma}}$) used a fixed β equal to 10. A continuation scheme on the η in this projection began when the inaccessible void constraint had been fully decremented, and η was increased in all 2D results by 0.05 every 15 iterations until $\eta=0.75$. The projection of the field $\psi-\hat{\tilde{\gamma}}$ in Equation (5) used $\beta=25$, $\eta=0.5$.

The grayness $\overline{\epsilon}$ was decremented from 1 at iteration zero every 25 iterations, and the inaccessible volume $\overline{\hat{V}}$ was decremented from iteration zero every 15 iterations. The initial value of $\overline{\hat{V}}$ was 10^{-3} for all fixed axis optimization, and ranged between 10^{-4} to 10^{-2} for variable-axis optimization.

Except for the case of $\mathbf{a}=0^{\circ}$, for single, fixed-axis experimentation only, the maximum allowable change in a nodal density variable value was increased from its nominal value of 0.2 to 0.5. While this caused oscillations during the initial iterations of the optimization, it aided in the avoidance of inferior local minima. Additionally, for single, fixed-axis optimization only aside from $\mathbf{a}=0^{\circ}$, the initial density distribution was specified to be unity (solid everywhere). For all other trials the initial density distribution was set to be the volume fraction. Aside from the $\mathbf{a}_{init}=0^{\circ}$ single, fixed-axis optimization which used a maximum angular move amount of 5° , all variable-axis optimizations used an angular move limit of 2.5° .

General parameter values for 2D are shown in Table 1 for brevity, where the appearance of values in the form χ_1 , χ_2 denotes a continuation scheme. χ_1 is the rate of increment or decrement and χ_2 is the minimum or maximum value of the parameter.

5.2.1 Reference design and fixed-axis numerical results

For 2D, a discretization with linear triangular elements was used and consisted of 4.5×10^3 nodes (density design variables). Figure 11 introduces the design problem and the reference result alongside the mesh used for all 2D optimizations.

In Figure 11A, the basic features of the 2D linear elasticity design problem are displayed. A point load is applied to end of a cantilevered beam, with a length twice that of its height. In Figure 11B, the reference result is shown, which does not consider manufacturability. The relatively intricate structure contains numerous internal voids and is clearly

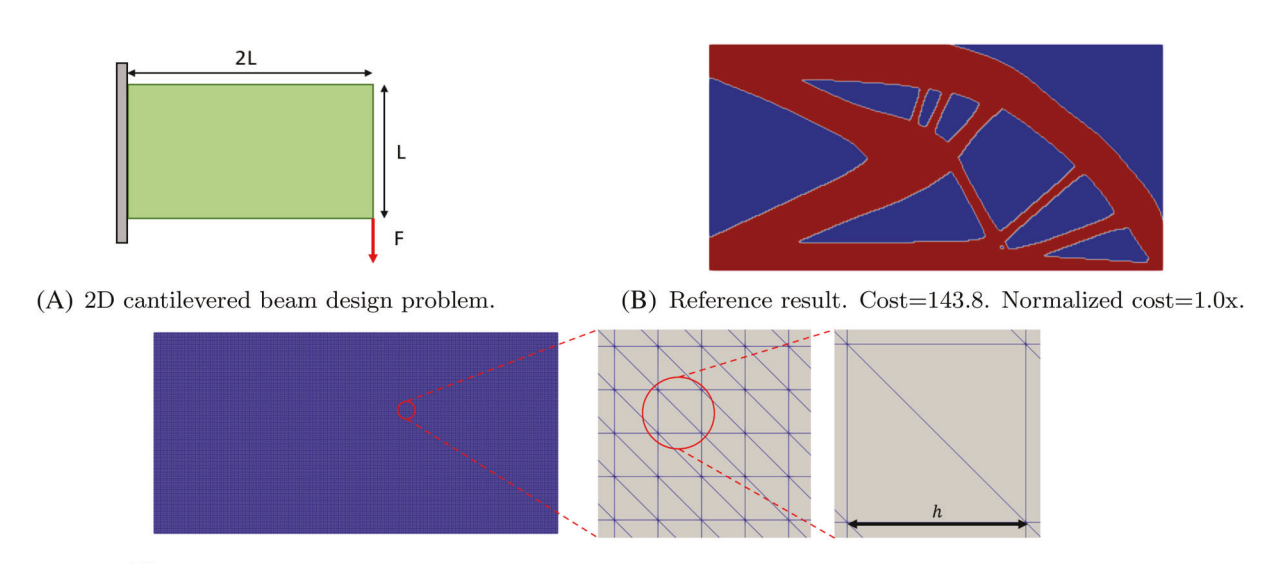
TABLE 1 Summary of continuation scheme parameters in 2D

Orientation	Axes present	Density Heaviside β	Grayness $\overline{\epsilon}$	$\overline{\hat{V}}$	Iterations
Fixed	Single	1.1-1.25, 9-11	$1.75, 5 - 20 \times 10^{-3}$	$3, 7.5 - 20^{-5}$	200-250
	Multiple	1.25, 11	$2, 10^{-2}$	$3, 10^{-4}$	150
Variable	Single	1.1, 9–13	$1.75, 7.5 - 20 \times 10^{-3}$	$2, 5 - 50 \times 10^{-5}$	225-250
	Multiple	1.1, 9	$2, 10^{-2}$	$2, 10^{-4}$	150

not manufacturable to any number and orientation of machine tools in the 2D plane. The compliance of the structure is 143.8, and all subsequent 2D designs will report a compliance normalized to this value. To help visualize the mesh and to clarify the definition of the element size, h which is required for the calculation of the PDE filter integral kernel, f_R , Figure 11C was created. Figure 11C illustrates, from left to right, the uniform 2D mesh, an enlarged view of the triangular elements, and an annotated mesh element showing h.

Figure 12 summarizes the results of four single, fixed-axis optimizations.

A few conclusions can be drawn from Figure 12. First, the enforcement of the manufacturability constraint yields geometric designs that are realizable by a single tool oriented in a specified direction. This statement is visually supported by the accessibility of all void regions in the physical design to a tool piece, originating from outside of the domain, moving in a specified direction. To reach and thus machine away material from the raw stock, this tool does not need to pass through a solid feature to reach a void volume. Second, it is clear from Figure 12 that an arbitrary enforcement of the single, fixed-axis implementation of this constraint sources significantly more compliant structures, ranging from more than 2.1× as compliant to almost 4.5× as compliant as the reference design.



(C) From left to right: 2D mesh, enlarged elemental-scale view of mesh, element size h.

FIGURE 11 2D Cantilevered beam, reference design, and 2D mesh

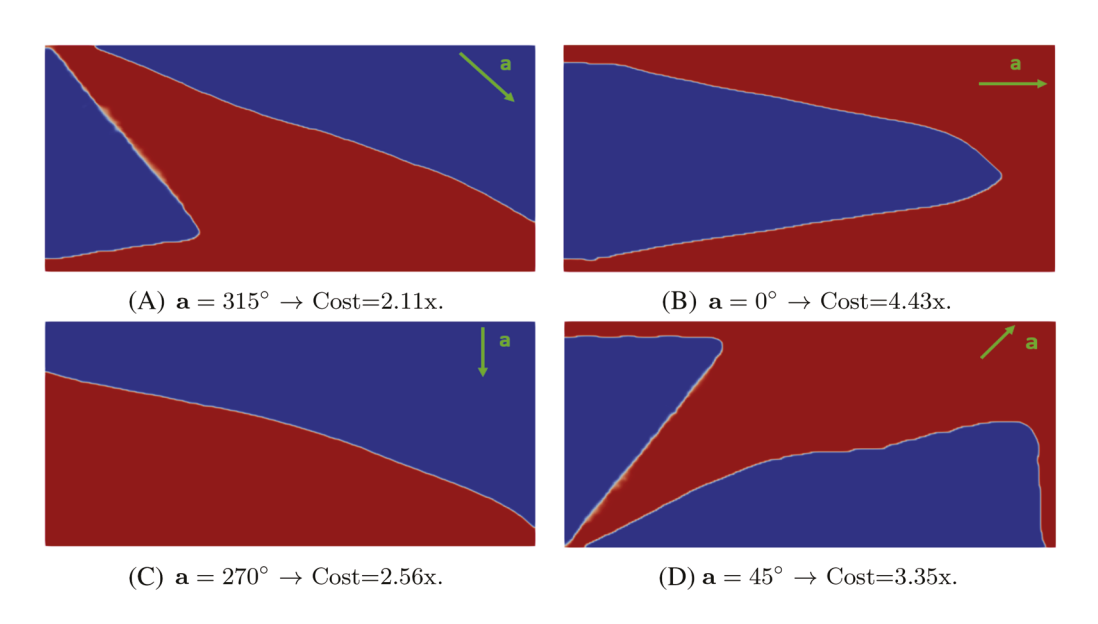


FIGURE 12 Single, fixed-axis optimizations at different machine axis orientations a

Inherently, the inaccessible volume constraint in Equation (5) offers two options for producing stiffer, equally manufacturable structures. One of these involves including additional pre-oriented axes in the machining operation, widening the design space for the optimization. This is exemplified in Figure 13, which compares a series of physical designs that could be produced from a multi-axis machining operation. In Figure 13, all machining orientations were chosen prior to the commencement of optimization and were constant throughout the optimization.

While the orientations in Figure 13 have still been arbitrarily chosen, in general the compliance of the structures is significantly lower than those shown in Figure 12. Reviewing Figure 13A with respect to Figure 12D shows that adding an additional axis oriented with $\mathbf{a}_2 = 225^\circ$ resulted in a decreased compliance of 36%. Including two additional axes, oriented along $\mathbf{a}_3 = 135^\circ$ and $\mathbf{a}_4 = 315^\circ$, as is shown between Figure 13A,C, decreased compliance by another 19%. One notable counterexample is the marginal increase and near-equality of the compliance of the designs in Figure 13B,D. This reduced stiffness from the former to the latter in spite of the presence of an additional axis can be attributed to two likely causes.

- 1. A consequence of the non-convex nature of the this optimization problem is that inferior local minima may exist and obstruct an optimizer from reaching a superior design. This characteristic is almost certainly exacerbated by the necessarily aggressive usage of exponential terms, which add to the non-linearity of the problem.
- 2. The scope of Table 1 and indeed the specificity of numerical parameters present throughout this implementation suggest that the underlying numerical scheme used to form the presented designs is not necessarily unique nor optimal. The authors believe that higher-performance designs may exist and may be elucidated through a different numerical scheme. The determination of such a scheme is considered to be beyond the scope of this article.

It is also worthwhile to compare the results presented in Figures 12 and 13 to those returned from the study of similar design problems in References 12 and 22. The form of Figure 12C agrees well with an analogous design in Reference 12 which enforced the millability of a cantilever structure to a single machine tool moving with the same orientation as was used to obtain Figure 12C. Different design domain dimensions hinder a direct comparison of the structure's relative costs. Qualitatively, the structures shown in Figures 12A,B,D, and 13B,D are similar to those obtained in Reference 22 for single- and multi-axis, fixed-axis optimizations. In general, the results shown in Reference 22 tend to have comparable normalized costs with respect to their counterparts in Figures 12 and 13. However, a direct comparison between cost values is likewise limited as a result of differing meshes, density PDE-filtering radii f_R , numerical parameters, and continuation schemes between Reference 22 and the present work.

To better understand the presented multi-axis results and the extent to which each machine tool contributes to the form of the structure in Figure 13D, consider Figure 14. The purpose of these illustrations is to emphasize the relationship between the solution of the advection-diffusion equation and the manufacturability of a design and to investigate the contributions of each machine axis towards generating a machinable design. This figure was generated following the final

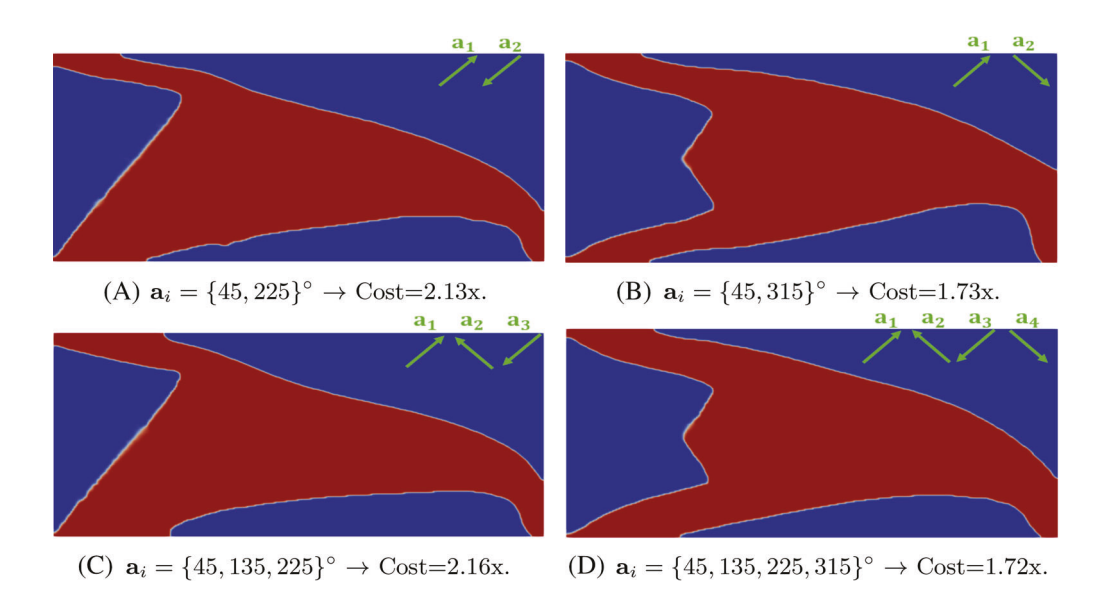
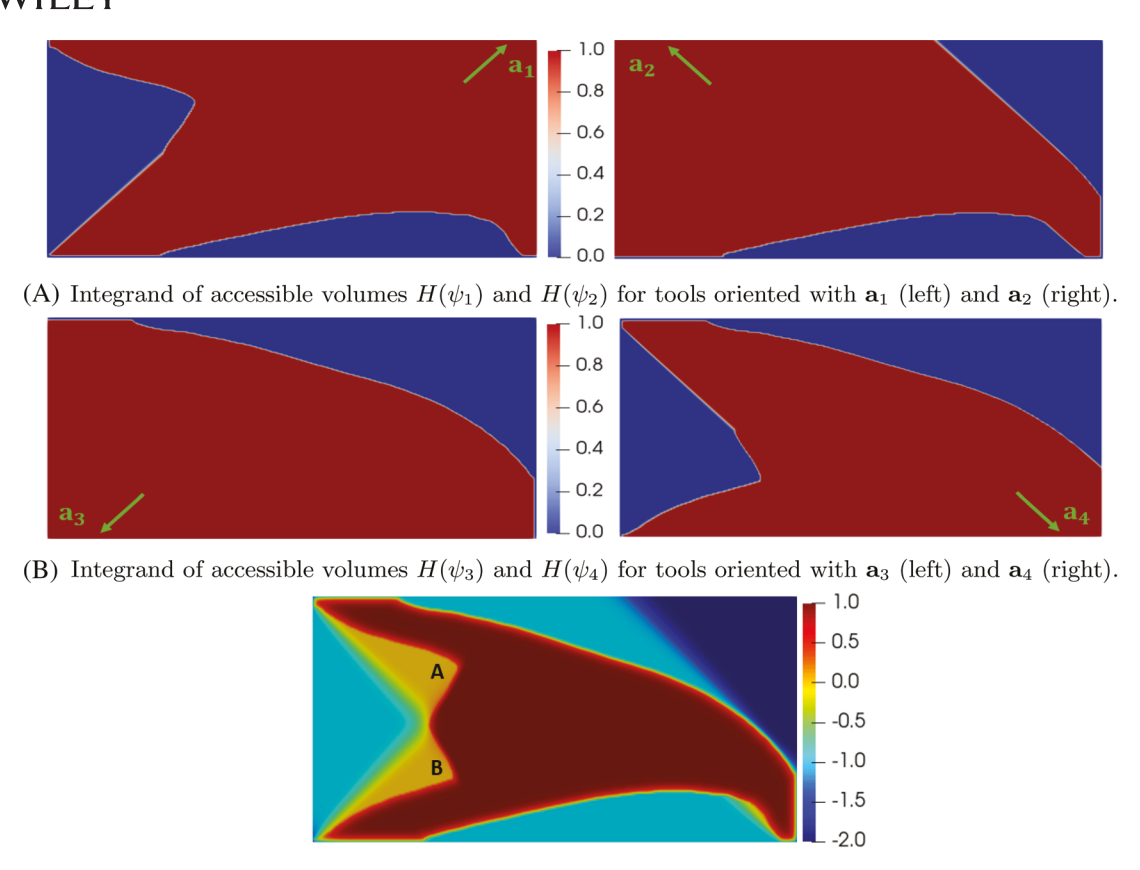


FIGURE 13 Multi-axis, fixed-axis optimizations



(C) Cumulative accessible volumes (volumes where the distribution is < 0) and inaccessible volumes (volumes where the distribution is > 0) for four machine tools.

FIGURE 14 Axis-specific accessible volume distributions in the multi-axis machining of the design in Figure 13D

iteration of the 4-axis, fixed-axis optimization shown in Figure 13D. In Figure 14A,B, a projection (for clarity) of the void volume of the final design that is accessible to each of the four tools individually is plotted (i.e., $H(\psi_i)$). Any void regions in Figure 14A,B are the volumes of a stock workpiece which a tool oriented along \mathbf{a}_i could access and machine away in an attempt to form the design in Figure 13D. Essentially, Figure 14A,B capture the extent to which a specific machine tool could realize Figure 13D in that the solid density in each figure would be the result of a machining operation on the stock workpiece by an individual tool. Figure 14C is a simple visualization of a token fabrication process that could form Figure 13D. Starting with a stock workpiece which has a density of unity everywhere, the accessible volumes specific to each of the four machine tools $\mathbf{a}_1 - \mathbf{a}_4$ have been subtracted. This is representative of each of the machine tools in turn machining material from the stock workpiece. Explicitly, the Figure 14C displays $1 - \Sigma_i (1 - \hat{V})$. Note the alternative color scale in Figure 14C is to avoid any confusion with intermediate value regions appearing as intermediate densities. All volumes in Figure 14C with a field value equal to or less than zero are accessible.

In the left figure in Figure 14A which plots the accessible volume for a machine tool moving with an orientation \mathbf{a}_1 , it is straightforward to recognize the volumes with field values near zero correspond to volumes in Figure 13D that the tool could access without passing through solid features of the design. For all machine axes \mathbf{a}_1 through \mathbf{a}_4 , only portions of the void regions demarcated in Figure 13D are individually accessible and as a result the design in Figure 13D is visually confirmed to be non-manufacturable to any one of the four axes. However, when considered collectively, as is shown in Figure 14C, all volumes in the physical density that are void and from a manufacturing perspective must be removed to elucidate the final design are accessible to at least one of the four tools. Volumes in Figure 14C that are relatively negative are accessible to a greater number of tools, while volumes that are accessible to only a single tool have a value near zero (such as the volumes annotated as \mathbf{A} and \mathbf{B}). It can be seen that the tools with orientations $\mathbf{a}_1 = 45^\circ$ and $\mathbf{a}_4 = 315^\circ$ are both critical for forming the design in Figure 13D, as each is associated with uniquely removing part of the stock workpiece to form Figure 13D. This may lend insight into the reason that the designs in Figure 13A,C are structurally inferior compared to the 2-axis design in Figure 13B. Despite the presence of an equal number of axes in Figure 13A compared to 13B and one

additional axis in Figure 13C, none of the machine tools in Figure 13A or B are able to access the region associated with volume $\bf B$ in Figure 14C. With the introduction of an axis with $\bf a=45^\circ$, this is removed from the designs in Figure 13B,D. The designs in Figures 13A,C commit material to volume $\bf B$ (in Figure 13C) and are forced to withdraw material from potentially structurally critical volumes. Essentially, the added axis in Figure 14C with respect to Figure 14A is unable to significantly contribute to forming a stiffer structure, as it only able to access a marginally wider range of physically relevant volumes in the evolving density. In both Figure 13A,C, the inability to remove material from the volume $\bf B$ in Figure 14C may partially explain the inferior performance of these designs.

A noteworthy feature of this discussion on the qualitative relative importance of axes in Figure 13 as well as directly from comparing the costs of the designs in Figure 13 is the lingering, artificial dependence of design performance on designer intuition. Even in a multi-axis environment, this hampers design performance. This may have been expected to be a salient feature of single-axis optimizations given the relatively significant restriction placed on the design space. However, a similar pattern emerges in the multi-axis results of Figure 13. Comparing Figure 13A,B, these two-axis optimizations yielded relatively unique structures and cost. The distinct structure in Figure 13B with respect to Figure 13A was obtained by simply re-orienting \mathbf{a}_2 from 225° to 315°, and the result was almost 19% less compliant. These statements motivate the utilization of the second option for producing stiffer designs in the original constraint formulation in Equation (5): the incorporation of the orientation(s) of machining into the topology optimization. By including the machining orientations as design variables in the optimization, it is possible to allow the orientation of the axes to organically develop in a similar manner to the topology and thus to fully move away from intuition-driven selections.

5.2.2 | Variable-axis numerical results

Figure 15 compiles a series of single-axis designs resulting from a manufacturability constrained optimization where the density and the machining orientation have been included as degrees of freedom. Each design in Figure 15A,C,D has an initial orientation \mathbf{a}_{init} corresponding to a fixed-axis optimization in Figure 12 to expedite discussion. To the left of all variable-axis optimizations, a plot of the initial orientation \mathbf{a}_{init} and the final, optimal orientation \mathbf{a}_{opt} have been included.

Figures 15A,C,D reveal the potential of the inaccessible volume approach to manufacturability constrained optimization. From comparing Figures 15A to 12A and 15D to 12B, it is apparent that including the axis of machining in the optimization is sufficiently freeing to prevent the formation of immediately inferior structures, with fixed- to variable-axis optimization cost decreases of 29% and 51%, respectively.

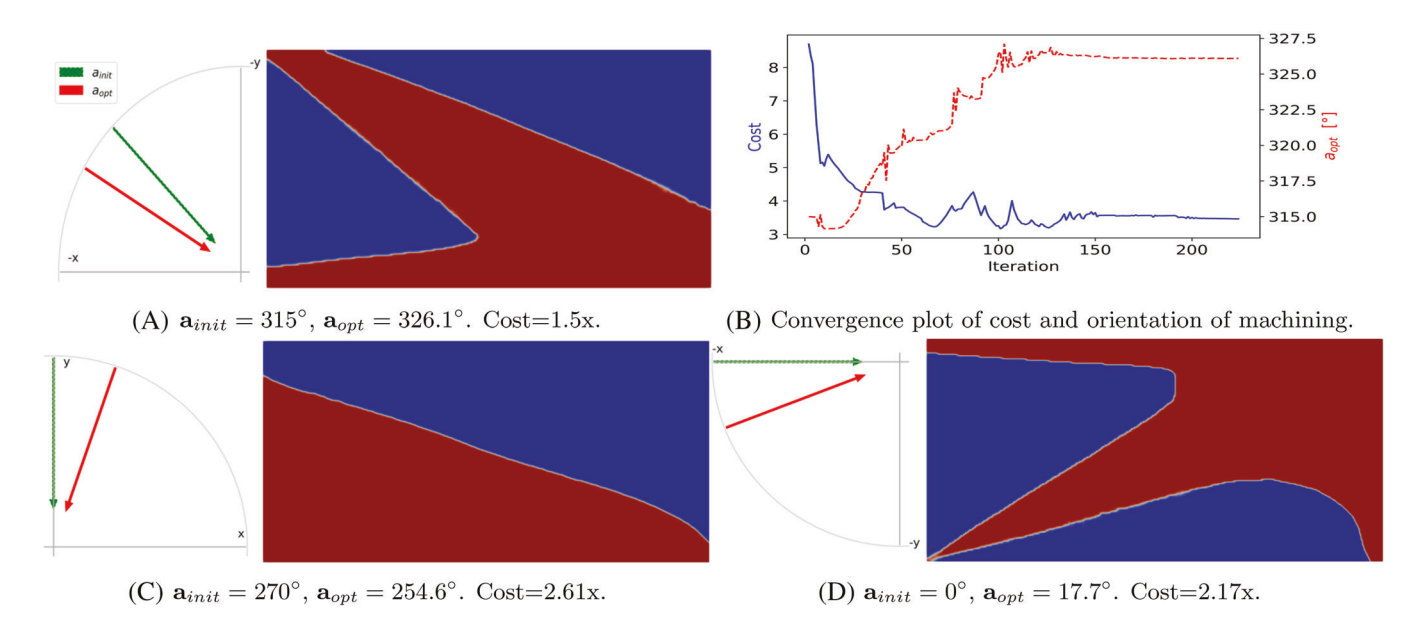


FIGURE 15 Single-axis, variable-axis optimizations. Orientation plots on the left of each design overlay the initial machine axis in green and the optimal machine axis in red

This encouraging statement is partially offset by the observation that three different results appear in Figures 15A,C,D and further the nearly-equal stiffness of the structures in Figures 15C and 12C. As was discussed following the results for the multi-axis optimization with pre-oriented axes and particularly in the context of several continuation schemes and parameter selections, the unique designs in Figure 15 and the marginally inferior performance of Figure 15C compared to Figure 12C is likely attributable to a sufficiently complex numerical landscape that precluded convergence to identical single-axis designs during the variable-axis optimizations.

As was expected, independently incorporating additional axes into the manufacturability constrained optimization and optimizing the density and orientation of machining simultaneously generally resulted in improved performance. Figure 16 incorporates both extensions on the single, fixed-axis optimization simultaneously. Note that Figure 16A uses the same initial orientations as the fixed-axis optimization in Figure 13A as does Figure 16B from Figure 13C.

Figure 16 displays a set of results that are more consistent with a priori expectations in that adding machine axes and including the orientation(s) of machining as design variables yield successively lower-cost structures. Figure 16A presents a structure with a cost 38% below that of its 2-axis, fixed-axis counterpart in Figure 13A. Including the orientations of machining in Figure 13C as design variables in the optimization similarly yields a significantly less compliant structure, shown in Figure 16B. It is also visually apparent that all three designs are organically more similar in form than the single-axis and multi-axis, fixed-axis optimizations that preceded them. Although the orientations of the three multi-axis, variable-axis optimizations are unique, the costs differ by between 2.5% and 6%. Although the orientations of the three multi-axis, variable-axis optimizations are not identical, the costs differ by a relatively small margin, between 2.5% and 6%. This point, when considered in conjunction with a simple visual review of Figure 16, is interesting in that it suggests that a variety of machining orientations could be used to form the designs in Figure 16, and that the reported machining orientations are not necessarily unique.

To streamline a review of the quantitative results of 2D fixed and variable, single and multi-axis optimizations results, Table 2 has been compiled. For all variable axis data in Table 2, the initial orientations of machining are identical to the fixed axis orientations shown in the same row.

The patterns that emerge from reviewing Figures 12,13,15, and 16 are manifold:

- Constraining the maximum inaccessible volume in a geometric design to zero is sufficient for ensuring the subtractive manufacturability of the product.
- In general, adding additional axes to the optimization improved cost, although this was shown to be contingent on the choice of axis orientation. Additionally, including the machining axes as degrees of freedom in the optimization yielded higher-performance designs.

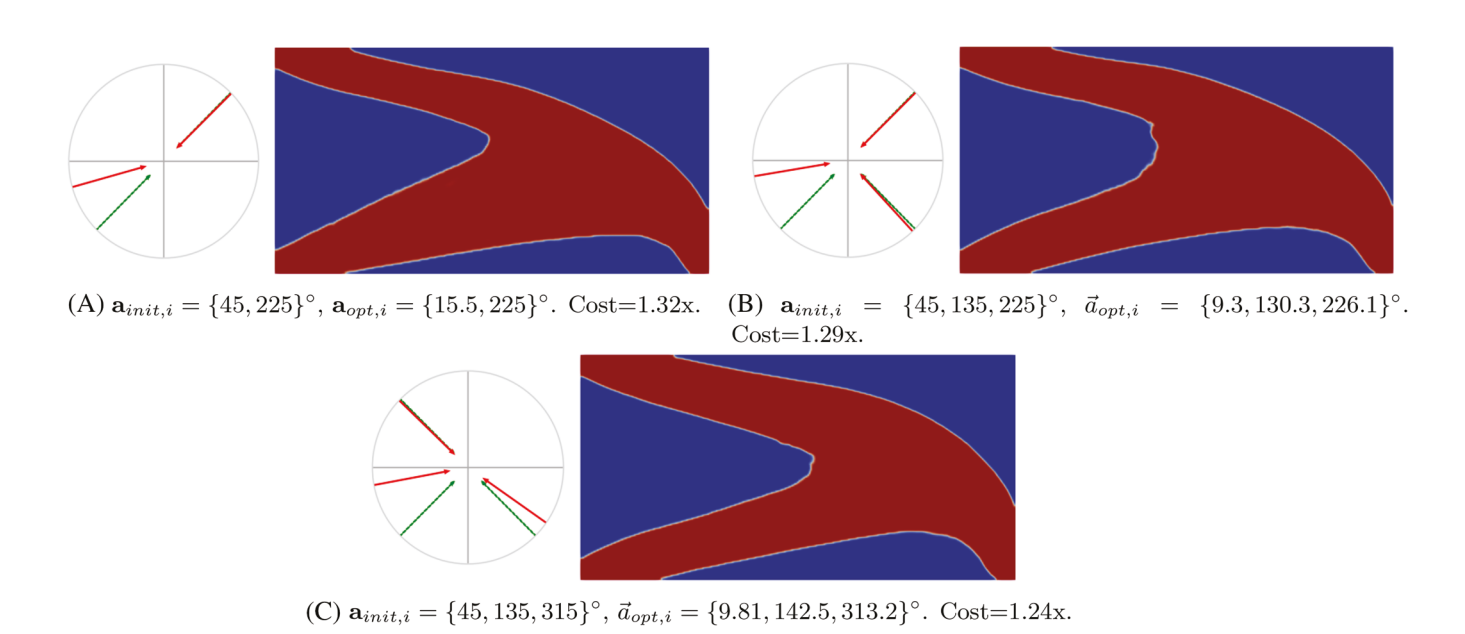


FIGURE 16 Three multi-axis optimizations where the machining axes have been optimized. Significant improvements in cost exist with respect to the fixed-axis equivalents previously presented in Figure 13

- A complex numerical landscape and specific numerical schemes impeded convergence to superior designs, even in a relatively reduced-size 2D design space.
- The approach is fully extensible to multiple axes.

5.3 | 3D numerical implementation and results

To investigate the efficacy of this method in a more practical setting, a 3D cantilever problem has also been addressed. Unless otherwise noted, numerical parameters are identical as those described for 2D. In 3D, convergence was assumed after 100 iterations. This assumption that was empirically supported by the convergence of the objective function prior to this iteration for all 3D optimizations.

For 3D results, the advection-diffusion equation used $\bar{\nu}=10^3$, $\beta_{\psi}=25\bar{\nu}$, with the source generation term being reduced to prevent overgeneration of darkness in solid regions of the physical density, which may have been a symptom of the refined mesh. Fixed axis optimizations invoked a density Heaviside at iteration 30 and variable axis optimizations did similarly at iteration 20 with the initial β set to 5. Incrementation of the density Heaviside β occurred every 10 iterations. The reprojection of the density through a Heaviside for manufacturability constraint evaluation in Equation (5) used a fixed β equal to 10 for fixed axis results and variable axis results. This projection η value was fixed at 0.5 for both fixed and variable axis optimizations. The projection of the field $\psi - \hat{\gamma}$ in Equation (5) used $\beta = 20$, $\eta = 0.25$, with the decreased η a response to the decreased source generation term.

The grayness $\overline{\epsilon}$ was decremented from 1 at iteration zero every 10 iterations for variable axis optimizations, and every 15 iterations for fixed axis optimizations. The inaccessible void \widehat{V} was decremented from iteration zero every 15 iterations, with an initial value of $\widehat{V} = 10^{-3}$. All variable-axis optimizations used an angular move limit of 2.5°.

General parameter values for 3D optimization are summarized in Table 3, and in the same manner as for Table 1, the appearance of values in the form χ_1 , χ_2 denote a continuation scheme. χ_1 is the rate of increment or decrement and χ_2 is the minimum or maximum value of the parameter.

5.3.1 | Reference design and fixed-axis numerical results

Linear tetrahedral elements were used to form a discretization of the design domain with 10⁶ design variables. A traction on the right-hand face of the beam was substituted for the point load applied to the lower right corner of the structure as

TABLE 2 Summary of numerical results in 2D

Fixed axis		Variable axis		
\mathbf{a}_i	Cost	$\mathbf{a}_{i,opt}$	Cost	
315°	2.11×	326.1°	1.5×	
0°	4.43×	17.7°	2.17×	
270°	2.56×	254.6°	2.61×	
45°	3.35×			
45, 225°	2.13×	15.5, 225°	1.32×	
45, 315°	1.73×			
45, 135, 225°	2.16×	9.3, 130.3, 226.1°	1.29×	
45, 135, 225, 315°	1.72×	9.81, 142.5, 313.2°	1.24×	

TABLE 3 Summary of continuation scheme parameters in 3D

Orientation	Axes present	Density Heaviside β	Grayness $\overline{\epsilon}$	$\overline{\hat{V}}$	Iterations
Fixed	Single, multiple	1.5, 25	$1.5, 5 \times 10^{-2}$	$1.75, 7.5 \times 10^{-4}$	100
Variable	Single, multiple	1.25, 20	$1.5, 5 \times 10^{-2}$	$1.75, 7.5 - 50 \times 10^{-4}$	100

was used in 2D. Subsequent designs have been extracted in accordance with $\overline{\tilde{\gamma}} > 0.5$. See Figure 17 for the design problem and corresponding reference cantilever structure.

The compliance of the reference structure, which does not consider manufacturability, is 140.0. All subsequent 3D results report a cost normalized to this value. In the rightmost perspective in Figure 17B, a slice through the middle of the reference design in the *x-z* plane reveals a series of internal voids.

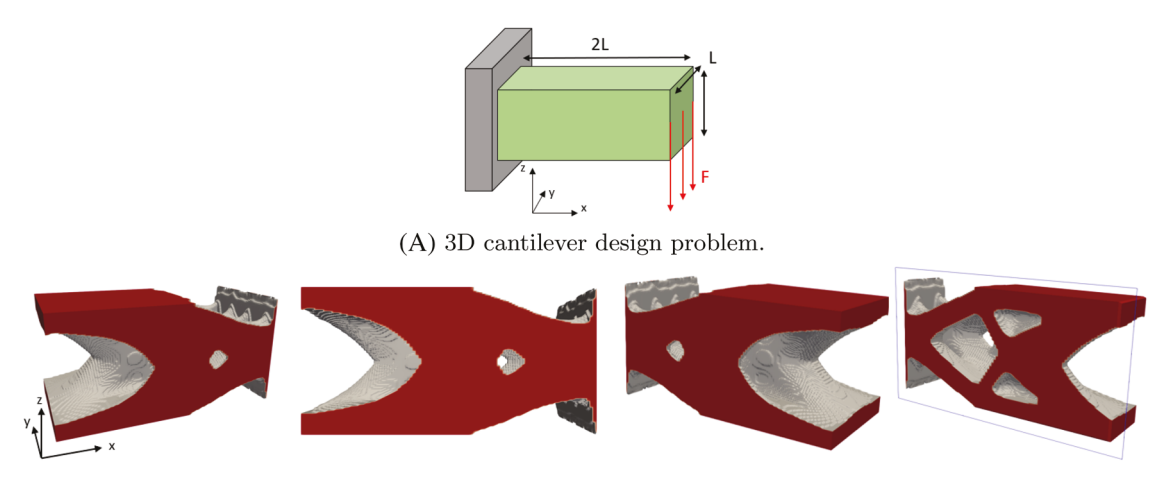
Using the same approach that was taken in 2D, a progression through the possible implementations of the inaccessible volume constraint will be used to structure the numerical discussion. Fixed-axis results for 1, 2, 3, 4, and 6 axes are shown in Figure 18.

Slices through design domain midplanes in Figure 18A–E reveal structures that are free from internal voids which is a self-evident prerequisite for a machinable design. The cost values reported in Figure 18 and the relative uniformity of the corresponding numerical parameters in Table 1 for 3D fixed axis experimentation contrast with the 2D results on a few points.

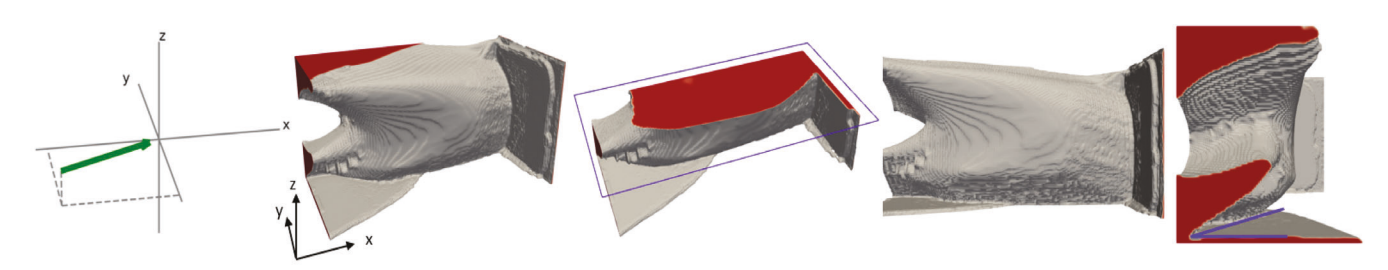
First, with the application of 2 arbitrarily selected axes, the normalized cost in 3D in Figure 18 is within 25% of the reference structure cost. A similar achievement in 2D required the incorporation of the orientations of machining into the optimization itself, although this statement is clearly dependent on the presented examples and is not necessarily expected to be universally valid. At a minimum, however, Figure 18B supports the idea that there may exist a relatively economical number of axes for which a manufacturability constrained optimization produces a result with only slight cost increase compared to a nominal structure.

Second, in a similar manner as in 2D, incorporating additional fixed axes such as between Figure 18A,B and 18B,C, led to successive decreases in cost of 33% and 7% respectively. This pattern held across Figure 18.

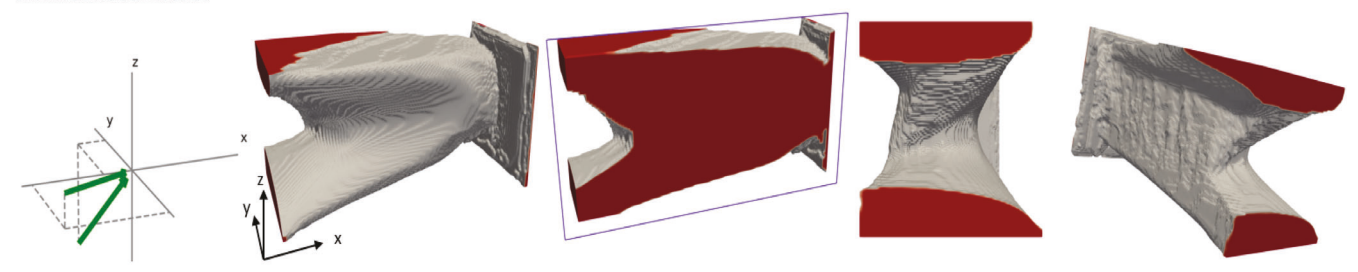
Third, Figure 18E evidences another application of the principle of a complex, non-convex numerical space precluding convergence to a superior minima. In 2D this may have contributed towards unique variable-axis optimization results. In a 3D context, the reference optimization itself may have converged to an inferior minimum as the inclusion of multiple, arbitrarily positioned axes yielded a stiffer design than the reference structure. It should be noted that the occurrence of manufacturability-constrained designs that outperform their non-manufacturability constrained reference structures has been previously documented (e.g., Reference 27, in an additive manufacturing context). Specifically for multi-axis machining, in Reference 22, a single, fixed machining axis optimization (essentially constraining the design to be manufacturable to 2.5D machining) was shown to have a cost within 5% of the reference design. Similarly to the investigation in 2D which focused on identifying the contribution of each machine axis to the final design, plots of accessible and inaccessible regions in a 3D environment can be generated. To add transparency to the functionality of the inaccessible volume method, the 6-axis case was selected for this demonstration to validate that all void volumes in the final design are accessible to at least one tool. Figures 19A–D display perspectives on the accessible volumes to individual machine axes, and Figure 19E presents a series of views of all accessible volumes, exploded along the axis of the corresponding machine tool. Conceptually, these volumes correspond to the void portions of the physical density in Figure 18E which are accessible to an individual tool. Equally, this would be the volume the stock workpiece that any given tool would be able to access



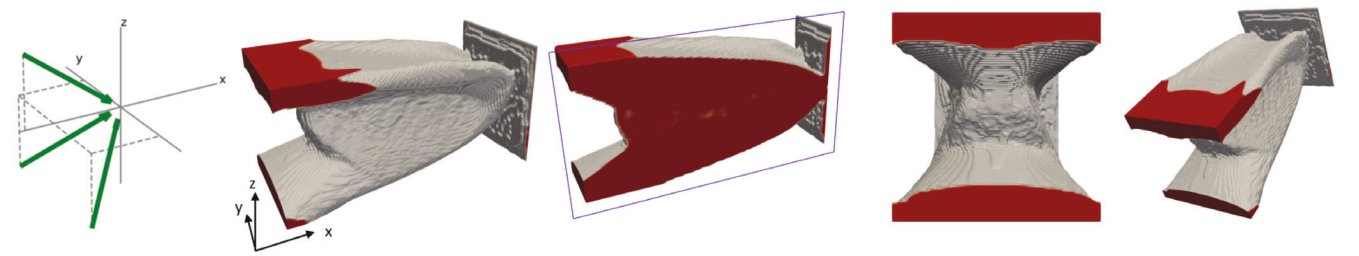
(B) Optimized structure, no consideration of manufacturability. Cost=140.0. Normalized cost=1.0x.



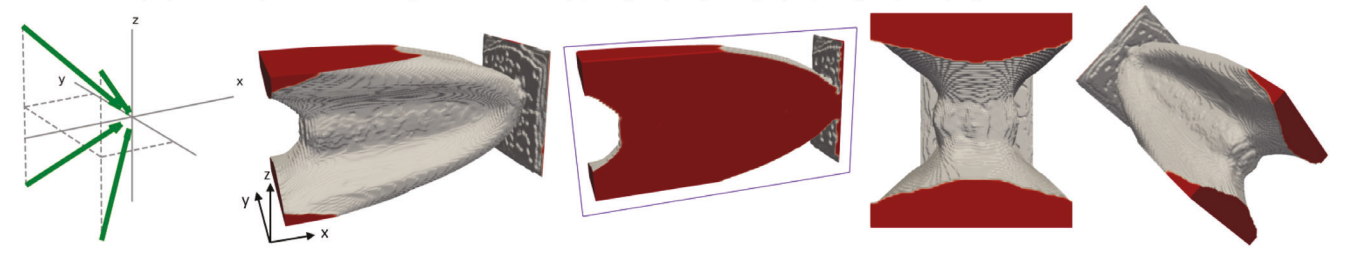
(A) Single, fixed-axis optimization. $\phi = 105^{\circ}, \theta = 45^{\circ} \rightarrow \text{Cost} = 1.88x$. The annotated angle in far-right perspective is 15° from horizontal (the same as the angle of approach of the tool piece), showing the overhanging structure is manufacturable.



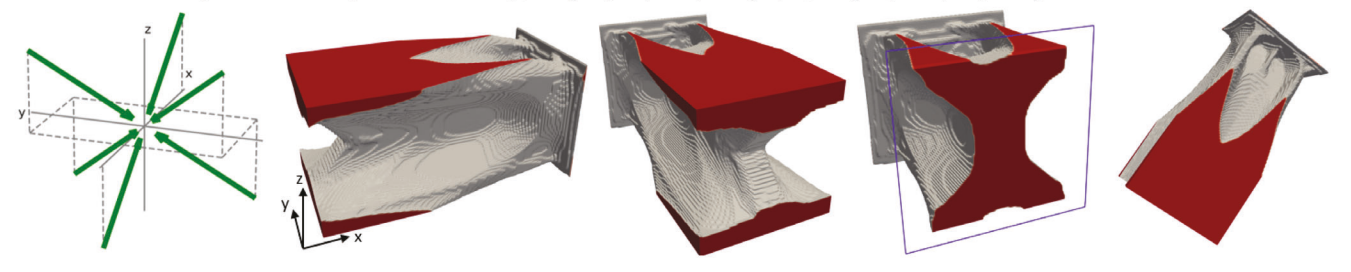
(B) 2-axis, fixed-axis optimization. $\phi_i \in \{105, 35\}^{\circ}, \ \theta_i \in \{45, 290\}^{\circ} \rightarrow \text{Cost} = 1.25x.$



(C) 3-axis, fixed-axis optimization. $\phi_i \in \{45, 45, 135\}^{\circ}, \theta_i \in \{45, 315, 0\}^{\circ} \to \text{Cost} = 1.16x.$



(D) 4-axis, fixed-axis optimization. $\phi_i \in \{45, 45, 135, 135\}^{\circ}, \theta_i \in \{45, 315, 45, 315\}^{\circ} \rightarrow \text{Cost} = 1.07x.$

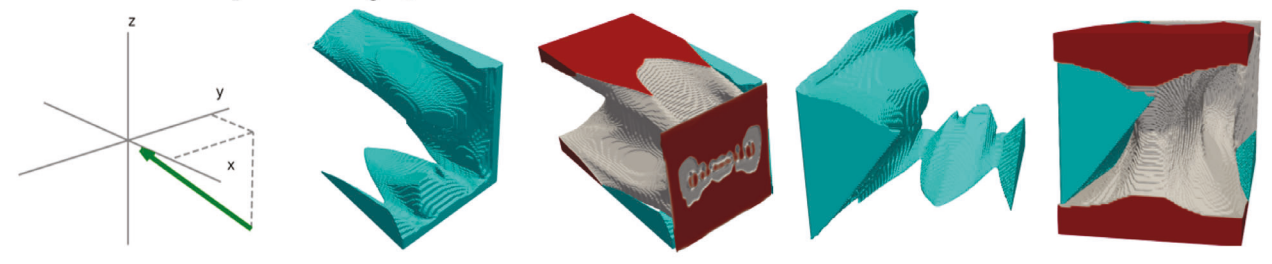


(E) 6-axis, fixed-axis optimization. $\phi_i \in \{45, 45, 45, 135, 135, 135, 135\}^{\circ}, \theta_i \in \{0, 120, 240, 60, 180, 300\}^{\circ} \rightarrow \text{Cost} = 0.96x.$

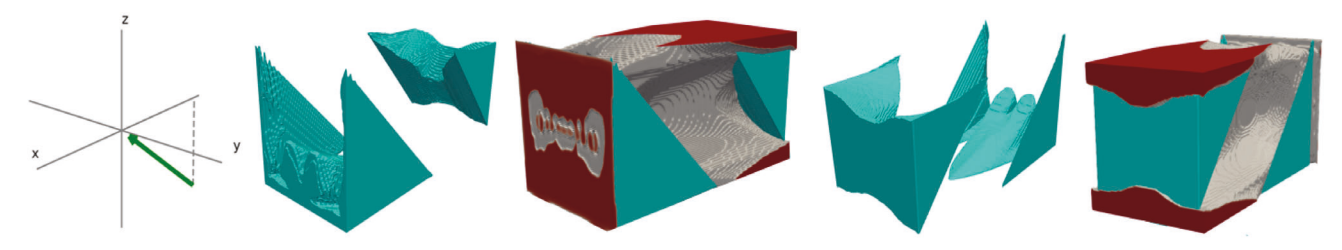
FIGURE 18 Fixed-axis, manufacturability constrained optimization in 3D. With the introduction of 6 axes, the compliance of the structure is less than that of the reference design



(A) \mathbf{a}_1 , two perspectives of the accessible volume of Figure 18(b) with respect to \mathbf{a}_1 , and two perspectives of these accessible volume exploded along \mathbf{a}_1 .



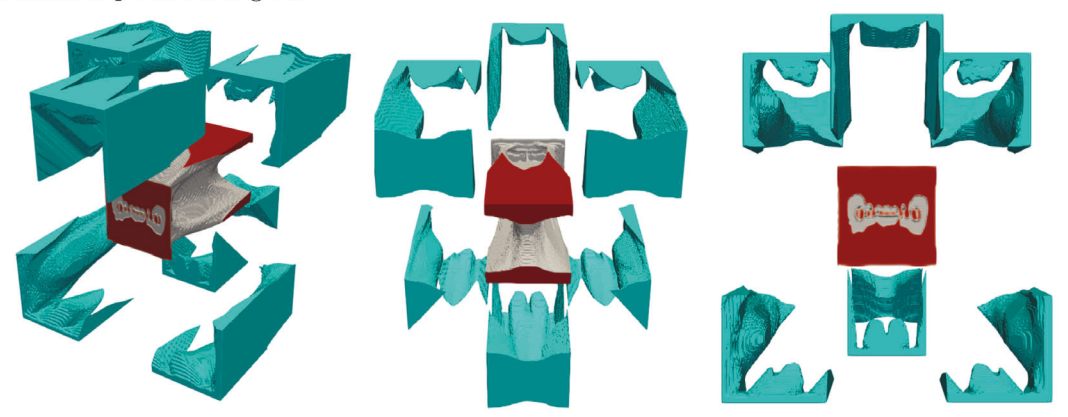
(B) \mathbf{a}_2 , two perspectives of the accessible volume of Figure 18(b) with respect to \mathbf{a}_2 , and two perspectives of these accessible volume exploded along \mathbf{a}_2 .



(C) \mathbf{a}_3 , two perspectives of the accessible volume of Figure 18(b) with respect to \mathbf{a}_3 , and two perspectives of these accessible volume exploded along \mathbf{a}_3 .



(D) \mathbf{a}_4 , two perspectives of the accessible volume of Figure 18(b) with respect to \mathbf{a}_4 , and two perspectives of these accessible volume exploded along \mathbf{a}_4 .



(E) Volumes accessible to each machine tool translated along the axis of machining.

and thus machine away without removing part of the solid physical design. The off-colored cyan volumes in Figure 19 relate directly to the blue volumes in Figure 14. Explicitly, these figures plot $1-\tilde{\gamma}-\hat{V}$, with \hat{V} the machine tool-specific inaccessible volume. Each subfigure contains a series of image. First, the orientation of one of the 6 axes is shown. Then, one perspective of the removable (accessible) volume specific to the machine axis is shown. This is followed by one perspective in which this volume is exploded from the original part (recognizable by its red outer surfaces) along the axis of the machine tool. It should be noted that near the front face of the design with respect to the x-axis, some perspectives do not show small isolated volumes as these tend to obstruct the view. Figure 19 is not intended to be an exact representation of the accessible volume, only a mechanism for illustrating the physical meaning of accessible and inaccessible volumes, and to lend general insight into the contributions of each tool to the final design in Figure 18E.

Figure 19 is useful for illustrating the extent to which each axis contributes to the design in Figure 18E and reinforces the physical meaning of the accessible and inaccessible volumes in a design. As the volumes being shown in Figure 19 are volumes accessible to each tool, as the inaccessible volume is constrained towards zero, all void volumes in the physical density must appear in one of these six plots. Summing the unique accessible volumes in Figures 19A–D will thus replicate the void regions of Figure 18E. It is evident that the six machine tools in tandem are able to access and machine away all void volumes in the physical density, and thus can form the specified part from the stock workpiece. It is also obvious that there is relatively significant overlap between the volumes that different tool pieces can access. For example, \mathbf{a}_1 and \mathbf{a}_3 are equally able to access volume near the bottom right corner of the fully loaded face, if one's perspective is along the positive x-axis. Additionally, tools oriented along \mathbf{a}_1 and \mathbf{a}_4 have equally free approaches to the right face of the design, enabling both to machine away volume from this portion of the stock workpiece. Therefore, it may be true that at least one of these axes could be somehow reoriented such that it has access to a unique and critical region of the evolving design and, as a result, that the performance of the design increases. To select such an orientation or to

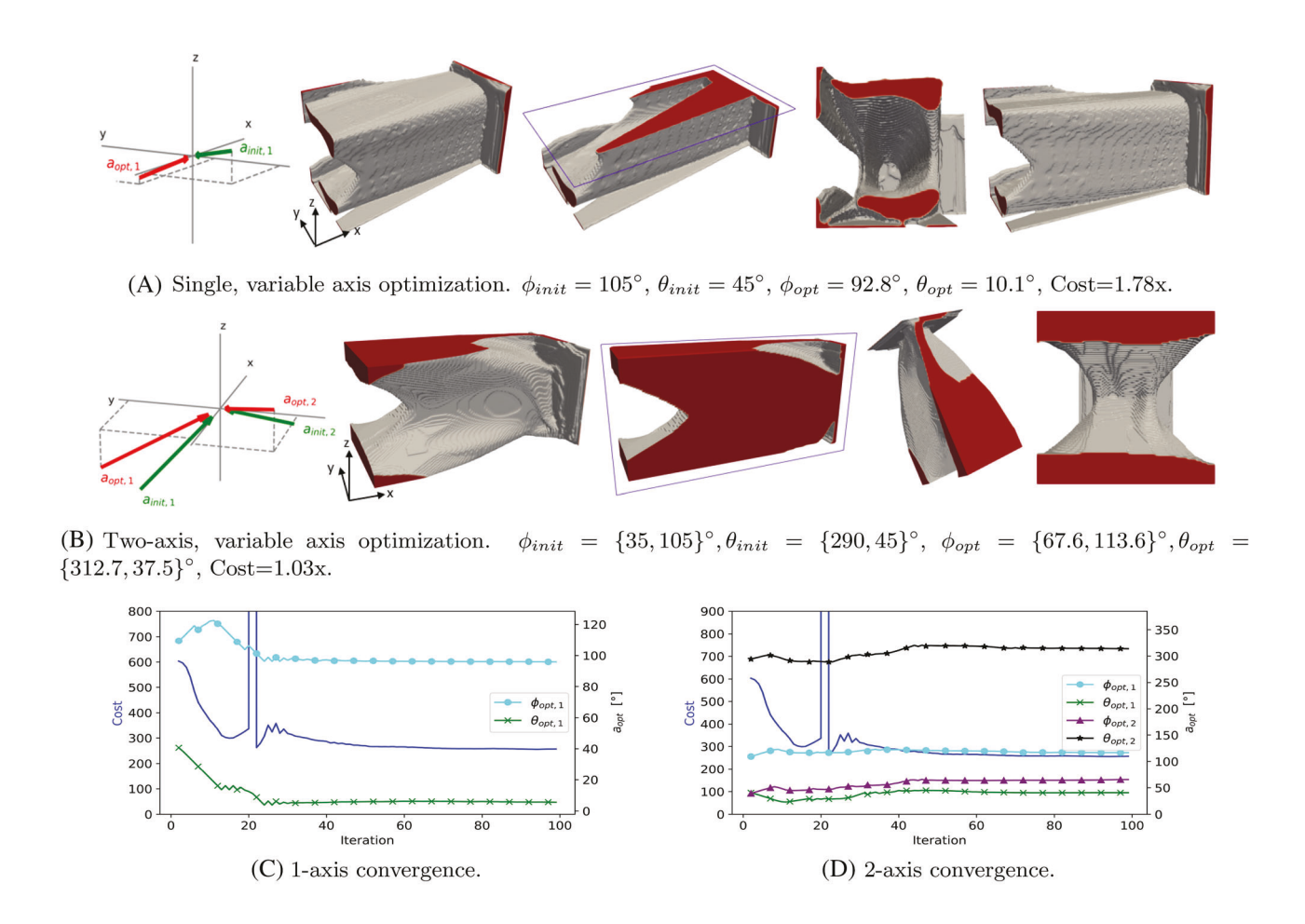


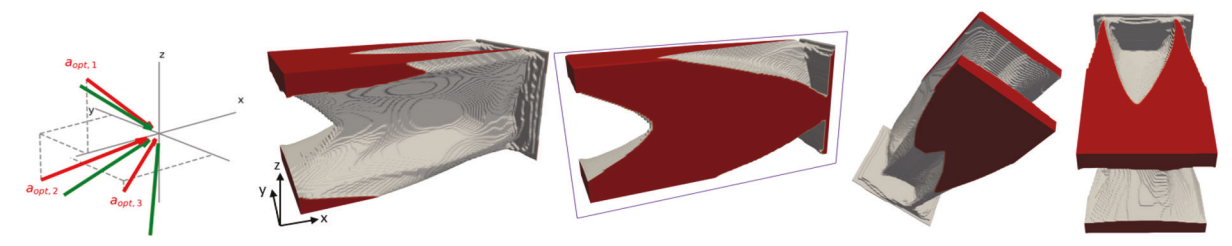
FIGURE 20 Variable-axis, manufacturability constrained optimization in 3D. With the introduction of a second axis, the optimized design is 3% more compliant than the reference structure

select such orientations a priori may be relatively challenging, however the inaccessible volume constraint differentiability with respect to the orientation(s) of machining allows for these to be optimized simultaneously with the density itself.

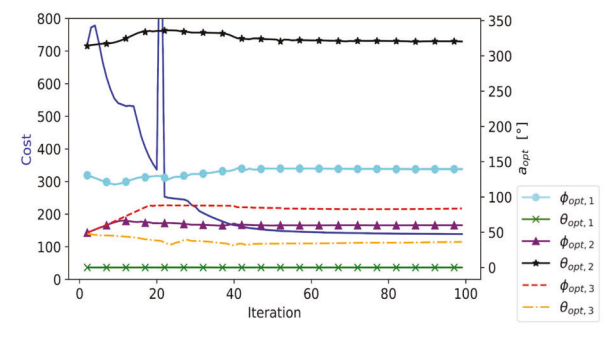
5.3.2 | Variable-axis numerical results

Despite the relatively convincing performance of the simple fixed-axis optimizations, including the orientations of the machining axes themselves in the optimization illustrates better illustrates the comprehensive capacity of this method for producing manufacturable, high-performance designs. Figure 20 shows the results of 1, and 2-axis, variable axis optimizations.

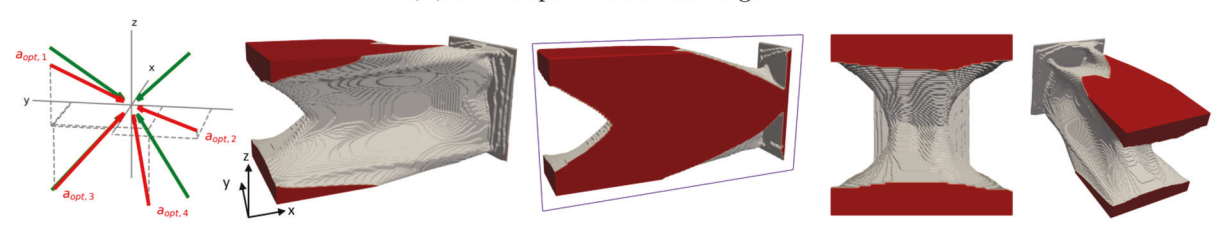
For the selection of initial machining orientations shown in Figure 20, the optimizations which included the axis or axes as degrees of freedom in the optimization yielded superior results compared to their fixed-axis counterparts. Cost decreases of 5% and 17% occurred between Figures 18A and 20A, and 18B and 20B, respectively. The design space became sufficiently free with the inclusion of a second axis such that the cost of the manufacturability constrained structure in Figure 20B was 3% more compliant than the reference design. The somewhat erratic behavior of the cost function during the early iterations coincides with the initiation of the continuation scheme for the Heaviside projection of the density ($\tilde{\gamma}$ to $\bar{\tilde{\gamma}}$). Given the relatively rapid recovery of the cost, this indicates a potential non-ideality in the numerical scheme which may be avoided under different implementations but did not necessarily adversely affect subsequent convergence of the cost or constraints.



(A) 3-axis, variable axis optimization. $\phi_{init} = \{135, 45, 45\}^{\circ}, \theta_{init} = \{0, 315, 45\}^{\circ}, \phi_{opt} = \{139.4, 59.8, 83.7\}^{\circ}, \theta_{opt} = \{0, 320.3, 36.2\}^{\circ}, \text{cost} = 0.99x.$



(B) 3-axis optimization convergence.



(C) 4-axis, variable axis optimization. $\phi_{init} = \{135, 135, 45, 45\}^{\circ}, \theta_{init} = \{315, 45, 315, 45\}^{\circ}, \phi_{opt} = \{126.2, 94.3, 50.3, 40.78\}^{\circ}, \theta_{opt} = \{325.3, 36.7, 324.1, 20.8\}^{\circ}, \cos t = 0.97x.$

FIGURE 21 3- and 4-axis, variable axis optimizations. Both structures have a compliance less than that of the non-manufacturability constrained reference structure

TABLE 4 Summary of numerical results in 3D

Fixed axis	Variable axis		
$\{\phi_i\}, \{\theta_i\}$	Cost	$\{\phi_{opt}, heta_{opt}\}$	Cost
{105}, {45}°	1.88×	{92.8}, {10.1}°	1.78×
{105, 35}, {45, 290}°	1.25×	{67.6, 113.6} , {312.7, 37.5}°	1.03×
{45, 45, 135}, {45, 315, 0}°	1.16×	$\{139.4, 59.8, 83.7\}$, $\{0, 320.3, 36.2\}^{\circ}$	0.99×
{45, 45, 135, 135}, {45, 315, 45, 315}°	1.07×	$\{126.2, 94.3, 50.3, 40.78\}, \{325.3, 36.7, 324.1, 20.8\}^\circ$	0.97×
$\{45, 45, 45, 135, 135, 135\}, \{0, 120, 240, 60, 180, 300\}^\circ$	0.96×		

Figure 21 increases the number of axes in the optimization to 3 in Figure 21A and 4 in Figure 21C to illustrate what further gains in cost are possible for this design problem. Additionally, Figure 21 can be used to investigate whether competitive results can be obtained between variable axis optimizations with relatively fewer axes and fixed axis optimizations with relatively more.

From Figure 21, as was true for the 6-axis, fixed axis optimization, the compliance of the manufacturability constrained structures decreased below that of the unconstrained structure. While all combinations, of fixed- and variable-axis orientations of machining were not explored, both methods support the conclusion that the scope and complexity 3D design space may be sufficiently extensive such that subtractive manufacturability constrained designs may approach to performance of unconstrained designs.

As was compiled for 2D, a summary of 3D results can be found in Table 4. Table 4 simplifies a direct comparison of fixed axis and variable axis results which use the same (initial) orientation of machining.

Upon review of all 3D results:

- The inaccessible volume approach is an effective manner for enforcing subtractive manufacturability in both 2D and 3D, for fixed and variable axes, and for single axis and multi-axis optimization.
- Including additional axes and incorporating the orientation(s) of machining in optimizations led to improved design performance.
- In 3D, a complex design space led to the repeated occurrence of manufacturability-constrained optimizations that outperformed the reference designs which did not consider manufacturability. This is due to the existence of multiple local minima in the design space.

6 | CONCLUSION

This article presents an approach for characterizing multi-axis machinability by a geometric measure: inaccessible volume. We give a formal mathematical definition for evaluating inaccessible volume in a density-based topology optimization. On a per-axis basis, inaccessible volume corresponds to a void region that exists behind a solid feature from the perspective of a tool. Constraining this volume to zero ensures that the design can be machined. A grayness constraint is introduced to prevent trivial, non-manufacturable, intermediate density solutions and exponential power terms has been added to the volume and grayness constraints to ensure their speedy convergence. Numerical examples on 2D and 3D linear elasticity problems evidenced the efficacy of the inaccessible volume constraint in ensuring the machinability of optimized designs. In general, incorporating the axis or axes of machining in the optimization resulted in a lower-cost design, although it was evidenced that a non-convex solution space in some optimizations led to convergence to inferior local minima. The 3D design space for the selected problem was shown to have sufficient scope and complexity such that both fixed axis and variable axis machinability constrained optimizations outperformed an optimized design without a machinability constraint.

Comments on future work

It is the author's intent to extend the presented approach from a simple linear elasticity environment to address more complex and immediately relevant problems. Namely, the author's believe the inaccessible volume method may be useful for a

variety of manufacturing and inspection modalities in which accessibility is a principal concern and has historically been a challenge to enforce. Examples of such applications include casting and milling, as well as touch probe- and laser-based coordinate-measuring machines or systems. Further, the author's believe this approach is extensible to multi-physics TO applications. These design problems offer the chance to couple the cost-effectiveness of subtractive manufacturing with the enhanced design performance that is achievable given the inaccessible volume's ability to include both the density and the machining orientations as degrees of freedom in an optimization.

Further, the shape of the tool piece is of interest in practical multi-axis machining applications, but tool shape was not explicitly considered in this formulation of the inaccessible volume constraint. Therefore an implicit assumption of this method and all results is that the smallest tool piece available for fabrication is at least as fine as the finite-element mesh. Refactoring the inaccessible volume method to consider tool cutter geometry is a potential extension of the present work.

ACKNOWLEDGMENTS

The authors would like to acknowledge the financial support from ONR grant N00014-18-1-2685 managed by Dr. Mark Spector and NSF grant 1941206. This work used the Extreme Science and Engineering Discovery Environment (XSEDE),³⁵ which is supported by National Science Foundation Grant number ACI-1548562.

DATA AVAILABILITY STATEMENT

The data that support the findings of this study are available from the corresponding author upon reasonable request.

ORCID

Xiaoping Qian https://orcid.org/0000-0002-9159-9877

REFERENCES

- 1. Bendsøe MP, Kikuchi N. Generating optimal topologies in structural design using a homogenization method. *Comput Methods Appl Mech Eng.* 1988;71(2):197-224. https://doi.org/10.1016/0045-7825(88)90086-2
- 2. Wu S, Zhang Y, Liu S. Topology optimization for minimizing the maximum temperature of transient heat conduction structure. *Struct Multidiscip Optim.* 2019;60(1):69-82. https://doi.org/10.1007/s00158-019-02196-9
- 3. Deng Y, Korvink JG. Topology optimization for three-dimensional electromagnetic waves using an edge element-based finite-element method. *Proc Royal Soc A Math Phys Eng Sci.* 2016;472(2189):20150835. https://doi.org/10.1098/rspa.2015.0835
- 4. Sun S, Liebersbach P, Qian X. 3D topology optimization of heat sinks for liquid cooling. *Appl Thermal Eng.* 2020;178:115540. https://doi.org/10.1016/j.applthermaleng.2020.115540
- 5. Høghøj LC, Nørhave DR, Alexandersen J, Sigmund O, Andreasen CS. Topology optimization of two fluid heat exchangers. *Int J Heat Mass Transf*. 2020;163:120543. https://doi.org/10.1016/j.ijheatmasstransfer.2020.120543
- 6. Bendsøe MP. Optimal shape design as a material distribution problem. Struct Optim. 1989;1(4):193-202. https://doi.org/10.1007/BF01650949
- 7. Xie Y, Steven G. A simple evolutionary procedure for structural optimization. *Comput Struct*. 1993;49(5):885-896. https://doi.org/10.1016/0045-7949(93)90035-C
- 8. Wang MY, Wang X, Guo D. A level set method for structural topology optimization. *Comput Methods Appl Mech Eng.* 2003;192(1-2):227-246. https://doi.org/10.1016/S0045-7825(02)00559-5
- 9. Bendsøe MP, Sigmund O. *Topology Optimization: Theory, Methods, and Applications*. Engineering Online Library. 2nd ed. Springer; 2011 OCLC: 711862335.
- 10. Simons M. Additive manufacturing—a revolution in progress? insights from a multiple case study. *Int J Adv Manuf Technol*. 2018;96(1-4):735-749. https://doi.org/10.1007/s00170-018-1601-1
- 11. Vatanabe SL, Lippi TN, de Lima CR, Paulino GH, Silva EC. Topology optimization with manufacturing constraints: a unified projection-based approach. *Adv Eng Softw.* 2016;100:97-112. https://doi.org/10.1016/j.advengsoft.2016.07.002
- 12. Guest JK, Zhu M. Casting and milling restrictions in topology optimization via projection-based algorithms. Proceedings of the American Society of Mechanical Engineers; 2012:913-920; Chicago, IL.
- 13. Gersborg AR, Andreasen CS. An explicit parameterization for casting constraints in gradient driven topology optimization. *Struct Multidiscip Optim*. 2011;44(6):875-881. https://doi.org/10.1007/s00158-011-0632-0
- 14. Liu J, Ma YS. 3D level-set topology optimization: a machining feature-based approach. *Struct Multidiscip Optim.* 2015;52(3):563-582. https://doi.org/10.1007/s00158-015-1263-7
- 15. Guest JK. Topology optimization with multiple phase projection. *Comput Methods Appl Mech Eng.* 2009;199(1-4):123-135. https://doi.org/10.1016/j.cma.2009.09.023
- 16. Li H, Li P, Gao L, Zhang L, Wu T. A level set method for topological shape optimization of 3D structures with extrusion constraints. *Comput Methods Appl Mech Eng.* 2015;283:615-635. https://doi.org/10.1016/j.cma.2014.10.006
- 17. Poulsen TA. A new scheme for imposing a minimum length scale in topology optimization. *Int J Numer Methods Eng.* 2003;57(6):741-760. https://doi.org/10.1002/nme.694

- 18. Wang F, Lazarov BS, Sigmund O. On projection methods, convergence and robust formulations in topology optimization. *Struct Multidiscip Optim.* 2011;43(6):767-784. https://doi.org/10.1007/s00158-010-0602-y
- 19. Qian X, Sigmund O. Topological design of electromechanical actuators with robustness toward over- and under-etching. *Comput Methods Appl Mech Eng.* 2013;253:237-251. https://doi.org/10.1016/j.cma.2012.08.020
- 20. Guest JK. Imposing maximum length scale in topology optimization. *Struct Multidiscip Optim*. 2009;37(5):463-473. https://doi.org/10. 1007/s00158-008-0250-7
- 21. Wang Y, Zhang L, Wang MY. Length scale control for structural optimization by level sets. *Comput Methods Appl Mech Eng.* 2016;305:891-909. https://doi.org/10.1016/j.cma.2016.03.037
- 22. Langelaar M. Topology optimization for multi-axis machining. *Comput Methods Appl Mech Eng.* 2019;351:226-252. https://doi.org/10.1016/j.cma.2019.03.037
- 23. Mirzendehdel AM, Behandish M, Nelaturi S. Topology optimization with accessibility constraint for multi-axis machining. *Comput-Aided Des.* 2020;122:102825. https://doi.org/10.1016/j.cad.2020.102825
- 24. Wang C, Qian X. Simultaneous optimization of build orientation and topology for additive manufacturing. *Addit Manuf*. 2020;34:101246. https://doi.org/10.1016/j.addma.2020.101246
- 25. Li Q, Chen W, Liu S, Tong L. Structural topology optimization considering connectivity constraint. *Struct Multidiscip Optim*. 2016;54(4):971-984. https://doi.org/10.1007/s00158-016-1459-5
- 26. Sato Y, Yamada T, Izui K, Nishiwaki S. Manufacturability evaluation for molded parts using fictitious physical models, and its application in topology optimization. *Int J Adv Manuf Technol.* 2017;92(1-4):1391-1409. https://doi.org/10.1007/s00170-017-0218-0
- 27. Qian X. Undercut and overhang angle control in topology optimization: a density gradient based integral approach: undercut and overhang angle control in topology optimization. *Int J Numer Methods Eng.* 2017;111(3):247-272. https://doi.org/10.1002/nme.5461
- 28. Sigmund O, Maute K. Topology optimization approaches: a comparative review. *Struct Multidiscip Optim*. 2013;48(6):1031-1055. https://doi.org/10.1007/s00158-013-0978-6
- 29. Bourdin B. Filters in topology optimization. Int J Numer Methods Eng. 2001;50(9):2143-2158. https://doi.org/10.1002/nme.116
- 30. Lazarov BS, Sigmund O. Filters in topology optimization based on Helmholtz-type differential equations. *Int J Numer Methods Eng.* 2011;86(6):765-781. https://doi.org/10.1002/nme.3072
- 31. Guest JK, Prévost JH, Belytschko T. Achieving minimum length scale in topology optimization using nodal design variables and projection functions. *Int J Numer Methods Eng.* 2004;61(2):238-254. https://doi.org/10.1002/nme.1064
- 32. Sigmund O. Morphology-based black and white filters for topology optimization. *Struct Multidiscip Optim.* 2007;33(4-5):401-424. https://doi.org/10.1007/s00158-006-0087-x
- 33. Kawamoto A, Matsumori T, Yamasaki S, Nomura T, Kondoh T, Nishiwaki S. Heaviside projection based topology optimization by a PDE-filtered scalar function. *Struct Multidiscip Optim*. 2011;44(1):19-24. https://doi.org/10.1007/s00158-010-0562-2
- 34. Svanberg K. The method of moving asymptotes—a new method for structural optimization. *Int J Numer Methods Eng.* 1987;24(2):359-373. https://doi.org/10.1002/nme.1620240207
- 35. Towns J, Cockerill T, Dahan M, et al. Xsede: accelerating scientific discovery. *Comput Sci Eng.* 2014;16(5):62-74. https://doi.org/10.1109/MCSE.2014.80

How to cite this article: Gasick J, Qian X. Simultaneous topology and machine orientation optimization for multiaxis machining. *Int J Numer Methods Eng.* 2021;122(24):7504-7535. doi: 10.1002/nme.6839

APPENDIX A. ADVECTION-DIFFUSION BOUNDARY CONDITIONS

The proposed boundary conditions on the advection-diffusion PDE, and those used to obtain numerical results are as follows:

$$\begin{cases} \psi = 0, & x \in \Gamma_D, \{\Gamma_D : \Gamma_D \subset \Gamma, \mathbf{n} \cdot \mathbf{a} \le 0\}, \\ \nabla \psi \cdot \mathbf{n} = 0, & x \in \Gamma_N, \{\Gamma_N : \Gamma \setminus \Gamma_D\}. \end{cases}$$

Here, the boundary conditions themselves are a function of the machining axis, that is, $\Gamma_N = \Gamma_N(\mathbf{a}_i)$ and $\Gamma_D = \Gamma_D(\mathbf{a}_i)$. The use of boundary conditions that are dependent in type and location on design variables may unnecessarily complicate the sensitivity analysis and as a result we choose to approximate the sensitivity of the constraint with respect to the manufacturing orientations by neglecting this aspect of the constraint sensitivity. To justify this decision, results obtained using the boundary conditions that are dependent on the machining orientation were compared with a set of results that used static boundary conditions. The objective of this empirical comparison is to show that similar designs with

competitive costs can be obtained through both types of boundary conditions, and that no arbitrary cost penalty is incurred from implementing the proposed set of boundary conditions and the associated simplified sensitivity derivation.

The alternative set of fully differentiable boundary conditions are summarized as:

$$\left\{ \psi=0,\qquad x\in\Gamma_{\psi}.\right.$$

In this formulation, the design domain Ω_{γ} is a subdomain of the advection-diffusion domain Ω_{ψ} , where Ω_{ψ} is an enlarged instance of Ω_{γ} . To solve for ψ over Ω_{ψ} , the density distribution is mapped "in place" from the design domain to the advection-diffusion domain. This mapping of the density defined in the design domain $\overline{\tilde{\gamma}}$ to the density in the Ω_{ψ} domain, $\overline{\tilde{\gamma}}_{\psi}$, can be described formally as:

$$\overline{\tilde{\gamma}}_{\psi}(x) = \begin{cases} \overline{\tilde{\gamma}}(x), & x \in \Omega_{\gamma}, \\ 0, & x \in \Omega_{\psi} \setminus \Omega_{\gamma}. \end{cases}$$

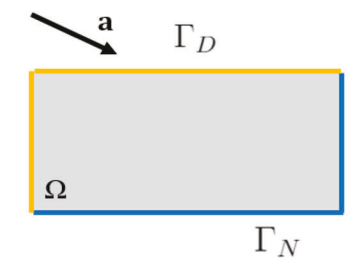
To evaluate the constraint and its sensitivity, the ψ field solved for in Ω_{ψ} is mapped back to the design domain to create ψ_{γ} . In this mapping, only when $x \in \Omega_{\gamma}$ is $\psi_{i,\gamma}(x)$ defined.

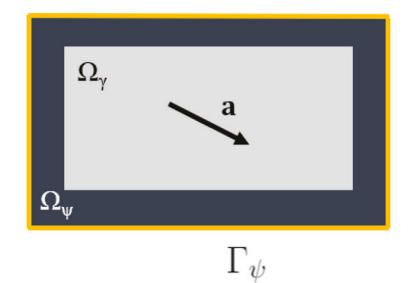
A visual comparison of the boundary conditions is shown in Figure A1.

In Figure A1A, the machining orientation and the domain normal are in directional opposition on the yellow-hued domain boundaries. Here, the illumination is fixed with $\psi=0$. All other boundaries are zero- ψ -flux boundaries, allowing for the free advection of generated ψ out of the domain. In Figure A1B, two alterations have been made. First, all boundaries are homogeneous Dirichlet boundaries. Second, the advection-diffusion domain Ω_{ψ} over which ψ is solved encompasses the design domain Ω_{γ} .

An enlarged advection-diffusion domain fulfills simultaneous needs for boundary conditions that (1) are independent of the direction of advection (2) do not undesirably influence ψ over the design domain. The former condition guarantees differentiability, and the latter ensures that ψ is free to evolve over the design domain to ensure proper constraint evaluation before redeveloping as required to satisfy the specified value at the domain boundary. To achieve both of these conditions, and to ensure the existence of a solution, the boundaries are chosen to be Dirichlet, and in particular, homogeneous Dirichlet boundaries.

A qualitative reason that suggests these seemingly-disparate numerical schemes will result in similar constraint performance is for the simple reason that the solutions to ψ for both schemes over the design domain should be nearly identical for any given advection direction. Boundary behavior over $\Omega_{\psi} \setminus \Omega_{\gamma}$ does not directly influence the inaccessible volume constraint evaluation over the design domain, and as a result when the mapping from $\psi \mapsto \psi_{\gamma}$ occurs, the distribution of ψ near a design domain boundary through which darkness is being advected is essentially equal for the two schemes. Further, when the advection direction is perturbed, both methods of solving for ψ return the similar results over Ω_{γ} , thus it may be permissible to approximate the sensitivity of the ψ distribution to the direction of advection using either scheme. As a demonstration of this idea and to support the practical equality of these two methods in solving for





(A) Proposed boundary conditions for ψ on Ω_{ψ} . Here, Ω_{ψ} (B) Alternative boundary conditions for ψ on Ω_{ψ} . Here, $\Omega_{\gamma} \subset \Omega_{\gamma}$.

FIGURE A1 Two types of boundary conditions for the advection-diffusion equation. In the left figure, the variable, mixed boundary conditions are illustrated. On the right, an alternative set of differentiable boundary conditions on Ω_w are shown

optimal topologies, both methods were implemented for a single-axis optimization in which the orientation of machining was included in the optimization as a degree of freedom.

Figure A2 compares the numerical results for two cases of variable-axis, machinability-constrained optimizations with the initial machining orientation of $\mathbf{a}_{init} = 45^{\circ}$ in Figure A2A,B and $\mathbf{a}_{init} = 45^{\circ}$ in Figure A2C,D.

Figure A2A–D compare the topology produced by optimizations under similar numerical parameters, with the left hand side Figure A2A,C implementing variable, mixed boundary conditions and the right hand side Figure A2B,D using static, homogeneous, all-Dirichlet boundary conditions on an enlarged domain Ω_{ψ} . The presented results are similar in structure, calculated optimal machining orientations, and cost. For both cases, the optimal cost differed by less than 3%, and the orientations by less than 6°.

The results shown in Figure A2 support two conclusions. First, the boundary conditions lead to different solutions even under similar numerical parameters, indicating that the sensitivity of the constraint to the machining orientation under mixed, machine orientation-dependent boundary conditions and all-Dirichlet boundary conditions are potentially unequal. Second, the designs are highly comparable, agreeing well in form and convergence. It is not possible to guarantee that one methodology will uniformly provide better results, yet the extent to which the topologies in Figure A2A–D agree assuages concerns about the usage of mixed boundary conditions during optimization. This demonstration is intended as an illustration of the potential of the two sets of boundary conditions to yield similar results, and clearly not as a formal proof of their equality.

Although this section has indicated that both boundary condition formulations are viable for use in machinability-constrained TO, the mixed, variable boundary conditions were implemented during the compilation of numerical results. This choice was due to the greater efficiency of the single-domain approach, which avoids both the demarcation of a domain and subdomain, and an unnecessary intumescence of the mesh to solve for ψ over an enlarged advection-diffusion domain. The latter was necessary to prevent disruptive oscillations in ψ in $\Omega_{\psi} \setminus \Omega_{\gamma}$ which may have influenced ψ over the design domain.

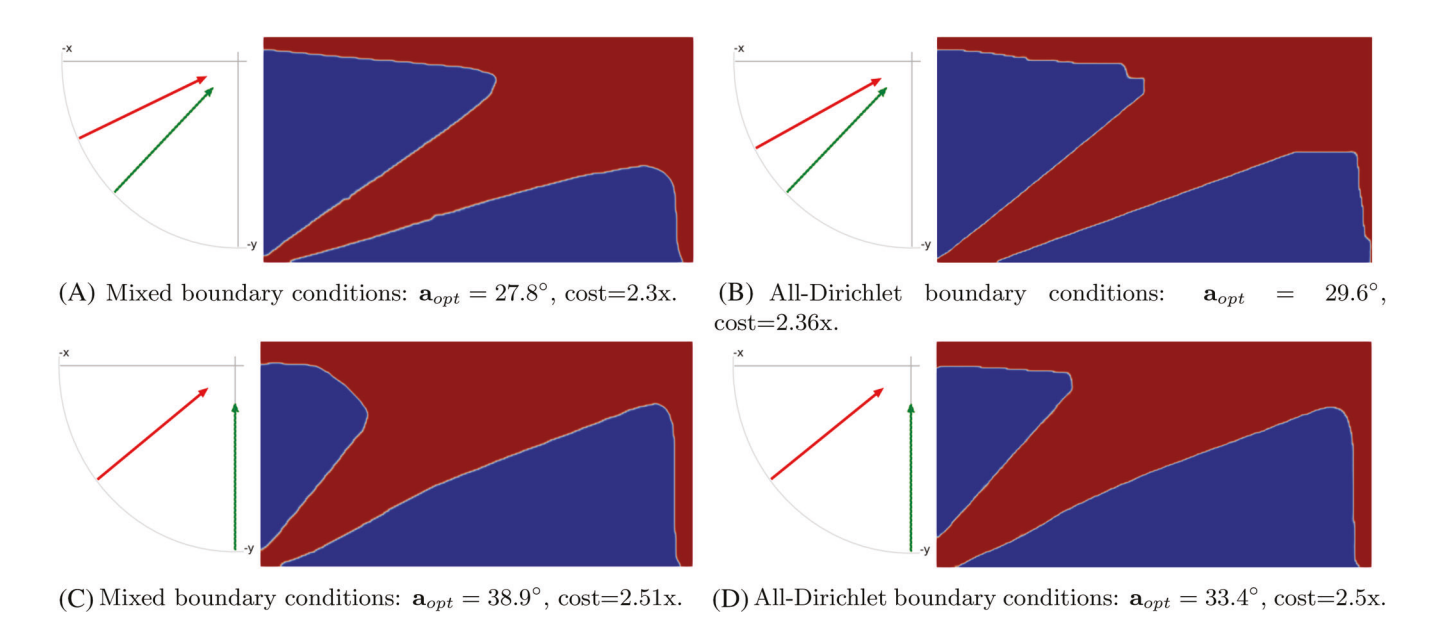


FIGURE A2 Two comparisons of potential boundary conditions. In the left figures, the boundary conditions of the advection-diffusion equation are functions of the machining orientation. On the right, the boundary conditions are enforced on an enlarged advection-diffusion domain and are homogeneous Dirichlet boundaries